African Journal of Engineering Research
Vol. 5(3), pp. 54-82, October 2017
ISSN: 2354-2144
Full Length Research Paper

Numerical experiments on glaciogenic artificial cloud seeding conducted in a stable cloud

Tsubasa Saito, Rocky Sashihara, Kennya Komatsuzaki and Kikuro Tomine*

Institute of Earth and Ocean Sciences, National Defense Academy, 239-8686, 1-10-20, Hashirimizu, Yokosuka, Kanagawa, Japan.

Accepted 26 September, 2017

ABSTRACT

The effectiveness of glaciogenic artificial cloud seeding is determined by two factors. One factor is whether ice crystals and liquid cloud water coexist in a cloud, resulting in water vapor deposit on the ice crystals growing them into snow particles. The other factor is whether convection is activated by released latent heat during freezing when water vapor deposits on the ice crystals. To investigate the influence of both factors and to research effective seeding methods using an aircraft, numerical experiments of glaciogenic artificial cloud seeding are conducted for a summer day when the cloud is relatively stable, resulting in little precipitation. Numerical results show that precipitation is increased in the catchment area due to glaciogenic seeding in regions of the cloud colder than 0°C, and the increase is enhanced when raindrops fall through areas of the cloud warmer than 0°C. Glaciogenic seeding can convert cloud water to snow and graupel to increase precipitation and activate convection. The activated convection can increase the amount of snow in the cloud; however, the convection also acts to separate the increased snow area from the cloud water area and the separation inhibits the formation of more snow particles. Multiple seeding can counteract this separation to enhance precipitation in the catchment area.

Keywords: Artificial glaciogenic cloud seeding, numerical simulation, weak rain, summer day.

*Corresponding author. E-mail: tomine@nda.ac.jp.

INTRODUCTION

Artificial cloud seeding is expected to be an efficient technique for weather modification and the redistribution of rainfall and snowfall, and has been widely tested to enhance rainfall intensity. Increased precipitation can be used in agriculture to alleviate poverty, and the augmentation of convective rainfall has been well studied (English and Marwitz, 1981; Woodley et al., 1982; Rosenfeld and Woodley, 1989). However, Hobbs and Politovich (1980) showed that artificial cloud seeding may not result in a significant increase in precipitation from cumulus complexes. Marwitz and Stewart (1981) showed that over-seeding could kill the cloud, though the reason was not known. In addition, randomized experiments have been carried out with inconclusive results (Rangno and Hobbs, 1995, 1997; Rosenfeld, 1997; Dennis and Orville, 1997; Bruintjes, 1999; Silverman, 2001; Garstang et al., 2004). Recently, Zoljoodi and Didevarasl (2013) statistically investigated the result of cloud seeding over the Yazd province in Iran during February, March, and April over 25 years (1973 to 1997) and confirmed the effectiveness of cloud seeding in this region. Moreover, to respond to extreme water shortages in southeast Queensland in Australia, the potential for cloud seeding to enhance rainfall was explored in Tessendorf et al. (2012), where it became clear that there was great variability in the natural cloud systems in the southeast Queensland region and that understanding this variability would be necessary before any conclusions could be made regarding the impact of cloud seeding.

Other effects of glaciogenic artificial cloud seeding include hail suppression and the control of snowfall from super-cooled clouds. The snowfall from a heavily seeded cloud was investigated by Holroyd and Jiusto (1971) with the aim to redistribute snow farther inland. They observed an increase in the snow crystal concentration, and the crystals' type was thick plates and solid columns

instead of rimed snow crystals. These results indicated that the seeded cloud had a dry environment. Miller et al. (1975) conducted a randomized cloud seeding project aimed at reducing hail damage, and showed that measurements of hail energy and hail depth derived from passive hail indicators on seed days were not so different from those on no-seed days, but the seeded storms had, on average, lower radar reflectivity factors, smaller hailstones, and lower hail energies. Hailstorm seeding experiments were also performed in Alberta, Canada, from 1980 to 1985 (Stewart, 1986). The results showed that the number of ice crystals in the seeded clouds was significantly greater than that in the unseeded clouds at their comparative stages in the cloud's life cycle. Increased numbers of ice crystals were initially observed only in a very small part of the cloud, but spread and increased with time. When the seeded feeder clouds were sufficiently distant from the main storm, the seeding was considered to have encouraged the early formation of precipitation particles. However, they failed to show clear evidence of the seeding in radar echo because of the low sensitivity of the radar. Tomine et al. (2015) conducted an experiment to show that massive seeding is effective in mitigating the damage caused by heavy snowfall. They formed a canal in a thick convective cloud by massive seeding, leaving the areas unaffected by seeding as a reference to show that the canal was formed by the massive seeding only and not by other factors. A part of the radar echo observed from onboard beneath the seeding track was weakened to divide the whole radar echo into two parts and the distribution of rainfall on the ground from the target cloud was confirmed to be divided into two distinct rates. Numerical simulations were used to show that the seeding resulted in rain particles accreting cloud ice and snow to form graupel particles. These graupel particles fell rapidly, thus temporarily intensifying the rainfall, which would subsequently decrease. Therefore, the weakened radar echo in the field experiment was deemed to be caused by the increase of rapidly falling graupel particles (Shimada et al., 2016).

In general, artificial cloud seeding is roughly classified into two categories: hygroscopic seeding and glaciogenic seeding. Hygroscopic seeding enhances precipitation through the modification of warm rain processes by injecting small salt particles of 0.5 to 1.0 μm in diameter into a convective cloud using a pyrotechnic flare (Mather et al., 1997; Cooper and Bruintjes, 1997). The injected salt particles broaden the cloud droplet spectrum and increase and accelerate the collisions and coalescence processes of cloud droplets, causing them to grow into precipitation particles (warm rain processes). Thus, hygroscopic seeding is expected to be effective in subtropical areas in continental air-masses.

Glaciogenic seeding is the original cloud seeding method, and was first discussed in Schaefer (1946) and Vonnegut (1947), who showed that dry ice and silver iodide were effective agents for cloud seeding in a super-cooled cloud, and Fletcher (1962) who observed that super-cooled clouds with cloud top temperatures warmer than −10°C were characterized by a shortage of the ice crystals required for natural precipitation. Cold rain processes are characterized by the growth of ice particles consisting of ice crystal, rimed ice crystal, snowflake, graupel, and hailstone. Therefore, it is expected that super-cooled cloud particles floating in a cloud warmer than −10°C can be effectively converted into falling snow particles by the injection of sufficient artificially induced ice particles. This method is called the glaciogenic seeding method, and utilizes the heterogeneous and homogeneous nucleation mechanisms of the ice phase to enhance precipitation, mainly in the mid-latitudes or in winter. The graupel and snow particles melt in air warmer than 0°C to form rain droplets which is expected to be able to promote the collision and coalescence processes to increase the precipitation amount in the warmer cloud area below, as well as the formation of rain particles in warm rain processes.

The glaciogenic seeding method is believed to include one more process for enhancing precipitation than the hygroscopic seeding process. This process stimulates convection in a cloud warmed with the released latent heat from freezing. Fukuta (1996) described the effects of the released latent heat induced by a roll-up expansion of the twin horizontal ice-crystal thermals. Wakimizu et al. (2002) applied the glaciogenic seeding method using liquid carbon dioxide in a super-cooled cloud in post-frontal weather conditions. The seeded cloud was shown to develop based on the strengthening of the radar echo. Seto et al. (2011) conducted a glaciogenic cloud seeding experiment in a winter stratocumulus cloud and numerically simulated the cloud evolution. The effects of released latent heat in the seeded cloud were seen in the simulated results but the details of these effects were not investigated.

This study is motivated by the potential for glaciogenic cloud seeding to alleviate the water shortages which sometimes occur in summer in Japan. To investigate how the glaciogenic artificial cloud seeding method would perform in summer and to design glaciogenic seeding methods that are more effective for enhancing precipitation, some seeding methods were numerically simulated on a summer day with little rain. Artificial cloud seeding by an aircraft is assumed in this study, because seeding from an aircraft allows the seeding agent to be directly injected into a cloud, while seeding using ground-based equipment must consider the meteorological conditions between the equipment and the cloud base.

PRECIPITATION AMOUNT OVER A CATCHMENT AREA

In this study, four types of seeding method are investigated numerically. The first method is a

conventional one-time seeding method in the seeding area with a seeding agent comparable to 1 kg of dry ice, referred to hereafter as the weak seeding method. The second method represents the standard seeding approach, with a seeding agent comparable to 15 kg of dry ice in the seeding area, referred to hereafter as the ordinary seeding method. The third method uses 15 individual seedings with a seeding agent comparable to 1 kg of dry ice at 5-min intervals with the aircraft tracking the seeded cloud, referred to hereafter as the multiple seeding method. In the fourth method, a seeding agent comparable to 1 kg of dry ice is used, and is dispersed only in areas of the cloud with air temperatures colder than −8°C, to estimate the seeding effects using AgI as the seeding agent, because seeded AgI can generate a similar number of ice crystal nuclei as dry ice at temperatures of around −8°C.

The computational domain consists of the three regions shown in Figure 1. The outermost area consists of 193 × 167 grid points at 9 km intervals (d01), and the second area consists of 298 × 226 grid points at 3 km intervals (d02). The innermost area consists of 208 × 214 grid points at 1 km intervals (d03). The time steps for the three domains are 30, 15, and 4 s. The model has 60 vertical layers for the three domains.

The seeding was assumed to be conducted at 16:10 JST. The distribution of the accumulated precipitation amount for the analysis period of 90 minutes between 16:10 and 17:40 JST in Domain 3 in the case without any seeding (hereafter, called the control case) is shown in Figure 2. The seeding area and catchment area for a dam are shown by black and purple squares in the figure. Accumulated precipitation amounts of around 0.3 mm and less than 0.3 mm are observed in the north-western part of the seeding area and in the area between the seeding and the catchment area. An accumulated precipitation amount of 2.0 or 3.0 mm is also observed in the eastern part of the catchment area. This is the area with the maximum accumulated precipitation amount in this study. The positions of the two cross-sections are shown by the solid and dashed lines in the figure.

The accumulated precipitation amount and relative increase (increase compared to the control case (%)) in the catchment area over 90 min in the four seeded cases and the control case are shown in Table 1. It is shown that the relative increase in the multiply seeded case is the largest. Hereafter, the processes that produced the above results are investigated.

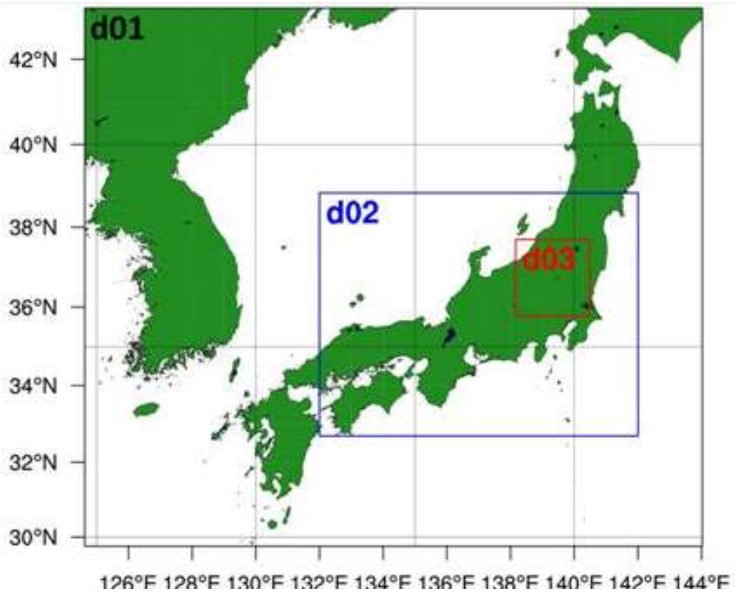

Figure 1. Computational domains. Black, blue and red rectangles in the figure show Domain 1 (d01), Domain 2 (d02), and Domain 3 (d03).

NUMERICAL MODEL

The Weather Research and Forecasting Model (WRF) version 3.7 was employed in this study. The Milbrandt 2-mon scheme for the cloud microphysics (Milbrandt and Yau, 2005a, b) was selected in the model. In the double moment scheme, both the mass mixing ratio and number density of six hydrometeor species are predicted. The six species used here are cloud droplets, cloud ice, snow, rain, graupel, and hail. The size distribution shape parameters and several other options can be specified. This model is known to produce distinct differences in storm structure, precipitation, and cold pool strength, especially in the early stages of storm development

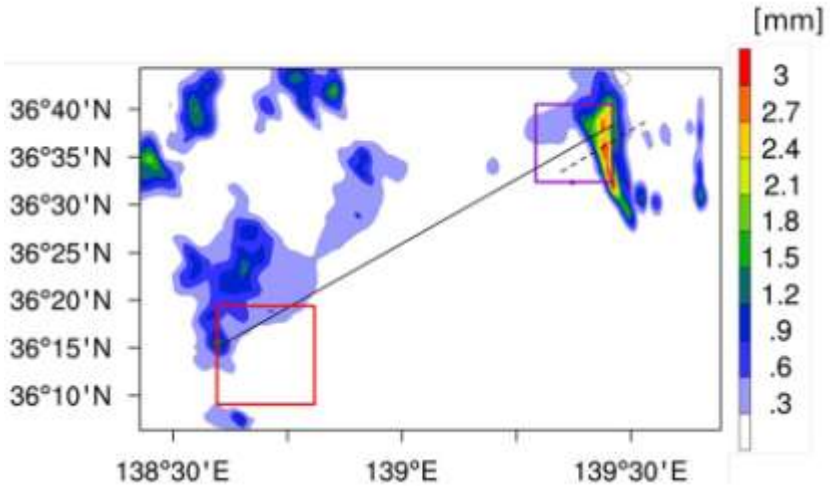

Figure 2. The distribution of accumulated precipitation amount for the analysis period of 90 minutes between 16:10 and 17:40 JSTs in Domain 3. Red and purple squares in the figure show the seeding area and a catchment area for a dam nearby. Positions of two cross-sections are shown by solid (Cross-section 1) and broken (Cross-section 2) lines in the figure.

Table 1. The accumulated precipitation amount (APM: mm) and relative increase (increase compared to the control case (%)) (RI: %) in the catchment area for 4 kind seeding methods.

	Control	Upper area seeded	Weakly seeded	Ordinary seeded	Multiply seeded
APM (mm)	0.86	0.92	0.97	1.05	1.11
RI (%)	0	7.0	12.8	22.1	29.1

(Morrison and Milbrandt, 2011).

Details of the model are presented in Table 2. The Mellor Yamada Nakanishi Niino 3 Scheme is adopted for the planetary boundary layer. The Rapid Radiation Transfer Model (RRTM scheme) (Mlawer et al., 1997) and Dudhia scheme are adopted for long-wave and short-wave radiation, respectively. The numerical simulation was performed for 18 h from 06:00 on June 16 to 00:00 JST on June 17, 2016. The initial and boundary conditions are formed from the objective analysis of the Meso-Scale Model output of the Japan Meteorological Agency. The sea surface temperature is formed from the Real-time Global Sea Surface Temperature Low Resolution analysis of the National Centers for Environmental Prediction.

The computational domains were set to allow an adequate approximation of the initial cloud conditions. We ran the model for 10 h and 10 min, from 06:00 JST to 16:10 JST to generate the initial cloud before seeding. Then the seedings were assumed to be conducted at 16:10 JST, except the multiple seeding method, and we analyzed the data for the 90 min between 16:10 JST and 17:40 JST. The seeding time and period for the analysis are shown in Figure 3. In this model, the effect of seeding is measured from the increases in the mass mixing ratio and number density of cloud ice, the increase in atmospheric temperature, and decrease of water vapor content corresponding to the released latent heat of deposition owing to seeding.

Seeding was assumed to be conducted along the seeding tracks in a seeding area of 20 km × 20 km shown in Figure 4. Dry ice was assumed to be injected as the seeding agent at a rate of 17 g per 100 m, meaning that 13.6 kg of dry ice was seeded in the study area. Cloud ice particles formed by the seeded dry ice were assumed to spread across the whole area instantaneously, and uniformly in the vertical direction from the cloud top to the level of 0°C with cloud water and to a width of 5 km in the horizontal direction regardless of wind direction.

Changes in the mass mixing ratio and number density of the cloud ice, increase in atmospheric temperature, and decrease in water vapor content corresponding to the deposition owing to the seeding were calculated as follows. One gram of dry ice is known to produce 10^{13} cloud ice particles (Fukuta et al., 1971). Then 1.36×10^{17} cloud ice particles (N_i) were estimated to be generated in the seeded area with 13.6 kg of dry ice as described above. In this case, the atmosphere was thermally stable and the cloud top was almost flat in the seeding area at

Table 2. Details of the numerical model

Used model	**WRF (ARW) Version 3.7**		
Initial and lateral boundary conditions	MSM of Japan meteorological agency (intervals of 3 hours)		
Sea surface temperature	NCEP RTG_SST_Low_Resolution		
Integration period	18 hours from 06 JST on January 16 to 00 JST on 17 June 2016		
	Domain1	Domain2	Domain3
Time steps	30 s	15 s	4 s
Horizontal grid interval	9 km × 9 km	3 km × 3 km	1 km × 1 km
Numbers of grid in the x-y plane	193 × 167	298 × 226	208 × 214
Numbers of layer	60 layers Top of the model is set at 100 hPa		
Cumulus parameterization	No		
Microphysics	Milbrandt 2-mom		
Planetary boundary layer	Mellor Yamada Nakanishi Niino 3 Scheme		
Surface layer	MYNN Scheme		
Land-Surface model	Thermal diffusion Scheme		
Long wave radiation	RRTM Scheme		
Short wave radiation	Dudhia Scheme		
Nesting	1 way-nesting		

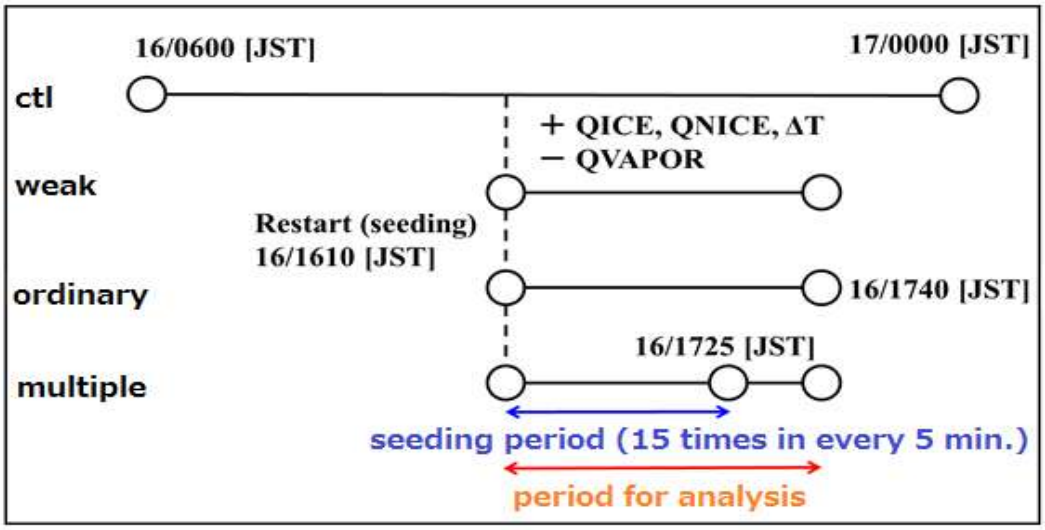

Figure 3. Layout of the seeding time and period for analysis. +QICE, +QNICE, ΔT, and -QVAPOR represent increases of mixing ratio and number density of cloud ice, warmed atmospheric temperature owing to deposition, and decrease of water vapor mixing ratio.

7.56 km height. Then the cloud ice was assumed to be spread across a volume of 1.32 × 10^{12} m^3 between heights of the cloud top and the 0°C level of 4.27 km and a seeding area of 20 × 20 km. The average air density (ρ) between these heights was 0.658 kg m^{-3}. Then, the number density increase of cloud ice (QN_i) owing to the seeding was 1.57 × 10^5 kg^{-1} based on the relation

$$QN_i = \frac{N_i}{\rho V}$$

.

The cloud ice particle was assumed to have a spherical shape with a radius of 6.45 μm and a density of 500 kg m^{-3}, resulting in a mass (M) of 5.62 × 10^{-10} g. Then, the increase of the cloud ice mass mixing ratio (Q_i) is 8.81 × 10^{-5} g kg^{-1}, as $Q_i = MQN_i$. The decrease of the water vapor mass mixing ratio (QVAPOR) is then $-Q_i$.

The increase in the atmospheric temperature (ΔT) corresponding to the released latent heat of the deposition caused by the seeding was calculated as

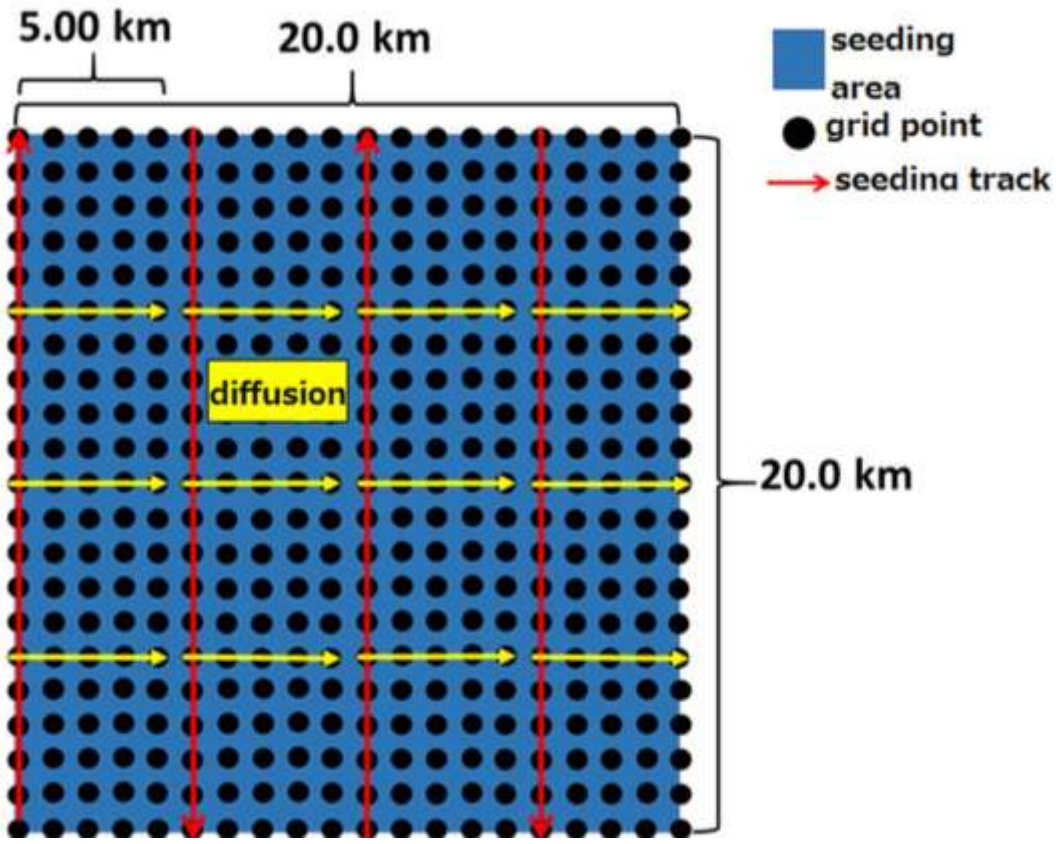

Figure 4. Positions of seeding tracks (red lines) and grid points (black circles).

follows. The latent heat of the deposition is expressed as $L_i = (2834.1 - 0.29T - 0.004T^2) \times 10^3$ (J kg^{-1}), where T is the atmospheric temperature (°C) (Rogers and Yan, 1989). The energy (Q Jkg^{-1}) required to increase the atmospheric temperature by ΔT is expressed by $Q = C_p \Delta T$, where C_p is the specific heat at constant pressure (= 1004 Jkg^{-1}K^{-1}). On the other hand, the released latent heat (Q Jkg^{-1}) from a deposition of Q_i water vapor is expressed by $Q = Q_i L_i \times 10^{-3}$. Then the increase in the atmospheric temperature (ΔT) was expressed by $\Delta T = \frac{Q_i L_i}{C_p}$. The average increase in the atmospheric temperature was 2.31 × 10^{-4}°C and thus negligible, although the increase varied depending on the grid point, because of differences in the atmospheric temperature.

SIMULATED CLOUD

A simulated cloud in the computational domain is necessary to conduct a numerical experiment on artificial cloud seeding. The visible satellite image and distribution of the numerically simulated vertically integrated cloud water quantity at 17:20 JST on June 16, 2016 are shown in Figure 5. Clouds are spread over Domain 3 and the vertically integrated cloud water quantity is between 0.6 to 1.0 kgm^{-2} in the southern area of Domain 3. The integrated cloud water quantity seems to show clouds that will produce little rain. The average precipitation rate and accumulated rainfall amount in Domain 3 (observed by the Automated Meteorological Data Acquisition System (AMeDAS)) are compared with those numerically simulated in Figure 6. The simulated precipitation rate and accumulated precipitation amount are less than those observed. However, these results seem to show sufficient accuracy to conduct numerical seeding experiments to enhance the total precipitation on a day with weak rainfall, though the distributions of the simulated vertically integrated cloud water quantity and total precipitation do not match the observations well.

Profiles of the atmospheric temperature and horizontal wind at 21:00 JST on June 16, 2016 are presented in Figure 7. The simulated atmospheric temperature is a little colder than the observed temperature overall, although the difference is less than about 2°C. Profiles of the simulated potential temperature and saturation equivalent potential temperature at 16:10 JST are shown in Figure 8. Cloud is simulated between heights of 3.8 and 7.5 km. The potential temperature increases with height for altitudes over 1 km. The vertical gradient of the saturation equivalent potential temperature is close to

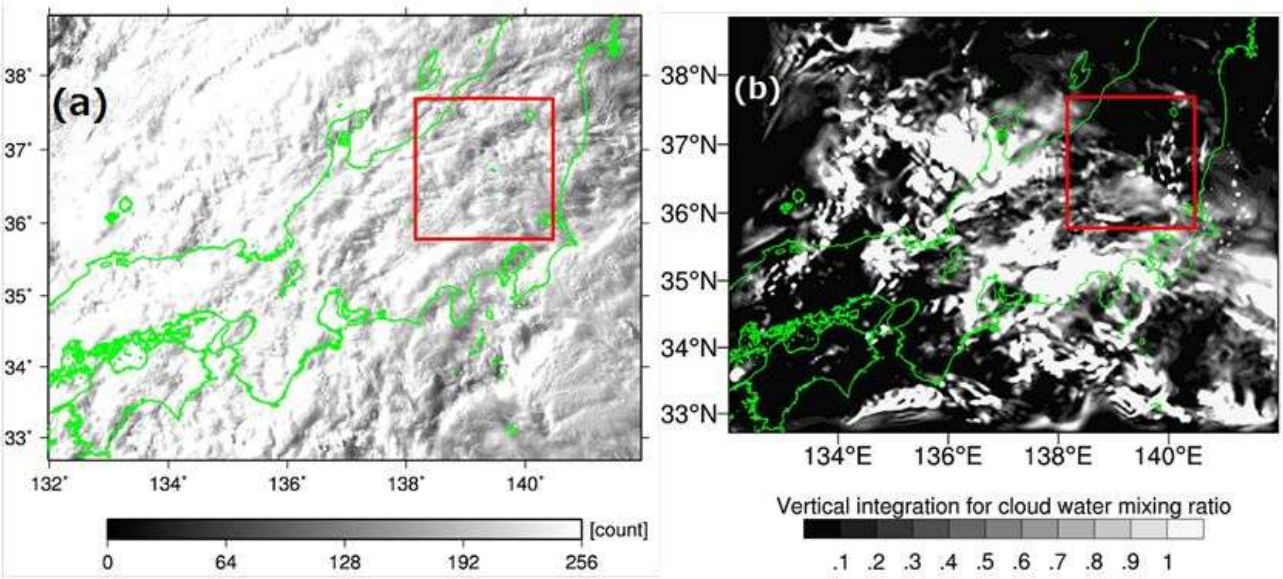

Figure 5. (a) A visible satellite image (brightness) and (b) distribution of numerically simulated vertically integrated cloud water quantity (kgm^{-2}) at 17:20 JST on 16, June, 2016. Red squares in the figures represent Domain 3.

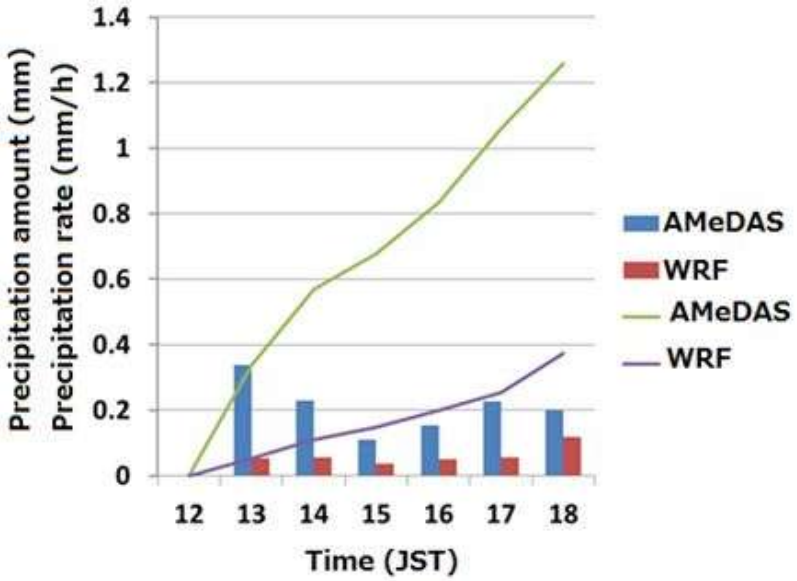

Figure 6. Comparison between average precipitation amounts observed by Automated Meteorological Data Acquisition System (AMeDAS) and simulated one. Average precipitation amount for one hour of 126 AMeDAS points in Domain 3 are used to calculate the average precipitation rate. Precipitation rate for one hour and accumulated precipitation amount are shown by bar and line graphs in the figure, respectively.

zero ($\frac{\partial \theta_e^*}{\partial z} \fallingdotseq 0$), but slightly positive, showing stable conditions, between the 4.7 and 6.7 km heights where cloud is simulated. The vertical gradient is positive ($\frac{\partial \theta_e^*}{\partial z} > 0$) in layers between heights of 2.0 and 4.7 km and over altitudes of 6.7 km. These conditions show that the simulated clouds are convectively inactive and strati-form type clouds. The profiles of the horizontal wind direction and speed are well simulated. The wind direction shows anticyclonic rotation with ascending height, suggesting warm air advection. Wind speeds near the cloud top at heights of 7.5 km and the cloud base at 3.8 km are about

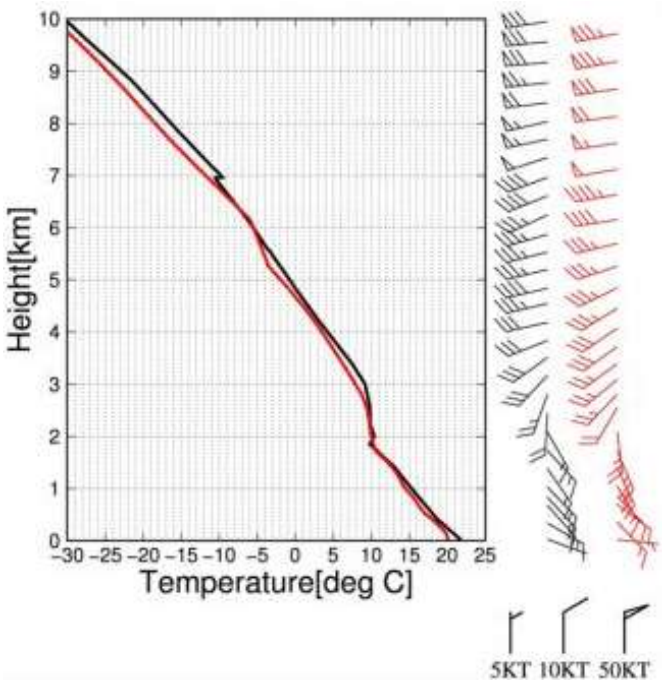

Figure 7. Profiles of atmospheric temperature and horizontal wind at 21:00 JST on 16 June, 2016. Black and red lines in the figure show observational and numerically simulated data. The observational point is Tateno which is about 70 km apart from the catchment area.

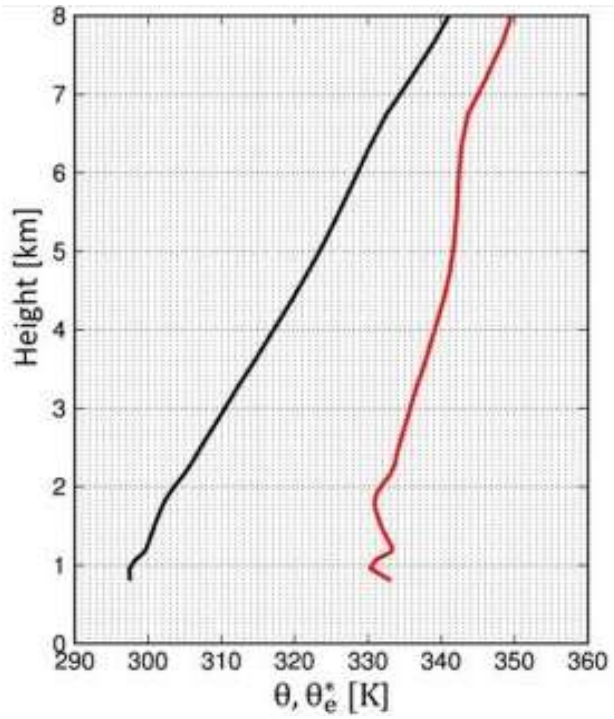

Figure 8. Profiles of simulated potential temperature θ and saturation equivalent potential temperature (θ_e^*) at 16:10 JST are shown by black and red lines in the figure.

55 kt (27.5 ms^{-1}) and 30 kt (15 ms^{-1}), respectively, and wind shear is observed there.

EVOLUTION OF CLOUDS WITHOUT SEEDING

The evolution of clouds without seeding (the control case) is analyzed here so that the effects of seeding can be quantified. The distribution of the surface wind is presented in Figure 9. The wind forms a convergent area in the eastern part of the catchment area, though there is a prevailing easterly or southeasterly wind. The convergence seems to arise from deformed wind due to the ground configuration, and the convergence area corresponds well with the area with an accumulated precipitation amount above 2 mm in Figure 2. The average wind speed at the cloud base height of 3.65 km around the seeding and the catchment areas is 13.7 m s^{-1} at 16:10 JST. Clouds in the vicinity of this area are expected to move at this speed (Hamada, 1979) and need about 62 min to move from the seeding area to the catchment area.

The distributions of the mass mixing ratios of cloud water, cloud ice, rain, snow, and graupel at the seeding time (16:10 JST) are shown in the cross-sections in Figure 10. The cross-sections are taken along line 1 in Figure 2. The seeding area is between 138.6°E and 138.8°E, and the eastern edge of the area is shown by the dash-dotted line in the figures. The cloud water mixing ratio, cloud ice mixing ratio, and graupel mixing ratio were 1.0, 0.0006 and 0.12 g kg^{-1}, respectively, over the seeding area. The rain mass mixing ratio extends to the ground over the seeding area, and there is no snow in this region. Therefore, the rain seems to be from melted graupel.

The distributions of the mass mixing ratios of rain droplets, snow particles, and graupel particles at 90 minutes after seeding (17:20 JST) are shown in the cross-sections in Figure 11. The right-hand side dash-dotted lines in the figures show the western edge of the catchment area. Rain reaches the catchment area at the time indicated in Figure 11a. Snow and graupel particles are found over the area as shown in Figure 11b and c, suggesting that the rain over this area is due to melted snow and graupel.

Cross-sections of the distributions of the cloud water mass mixing ratio and vertical wind component at 10, 20, 30, 40, 50 and 70 min after seeding are shown in Figure 12. The eastern tip of the cloud surrounded by a broken line is the position assumed to be seeded. This part of the cloud is moving eastward from the seeding to the catchment areas. The mass mixing ratio of cloud water in the simulated seeding area decreased from 1.0 to 0.6 g kg^{-1} in the period between 10 and 30 min after seeding (Figure 12a, b, c). The ratio then increases again to 1.0 g kg^{-1} at 40 min and the cloud top ascends by 0.5 km from 7.0 km to 7.5 km (Figure 12d) before descending to 7.0

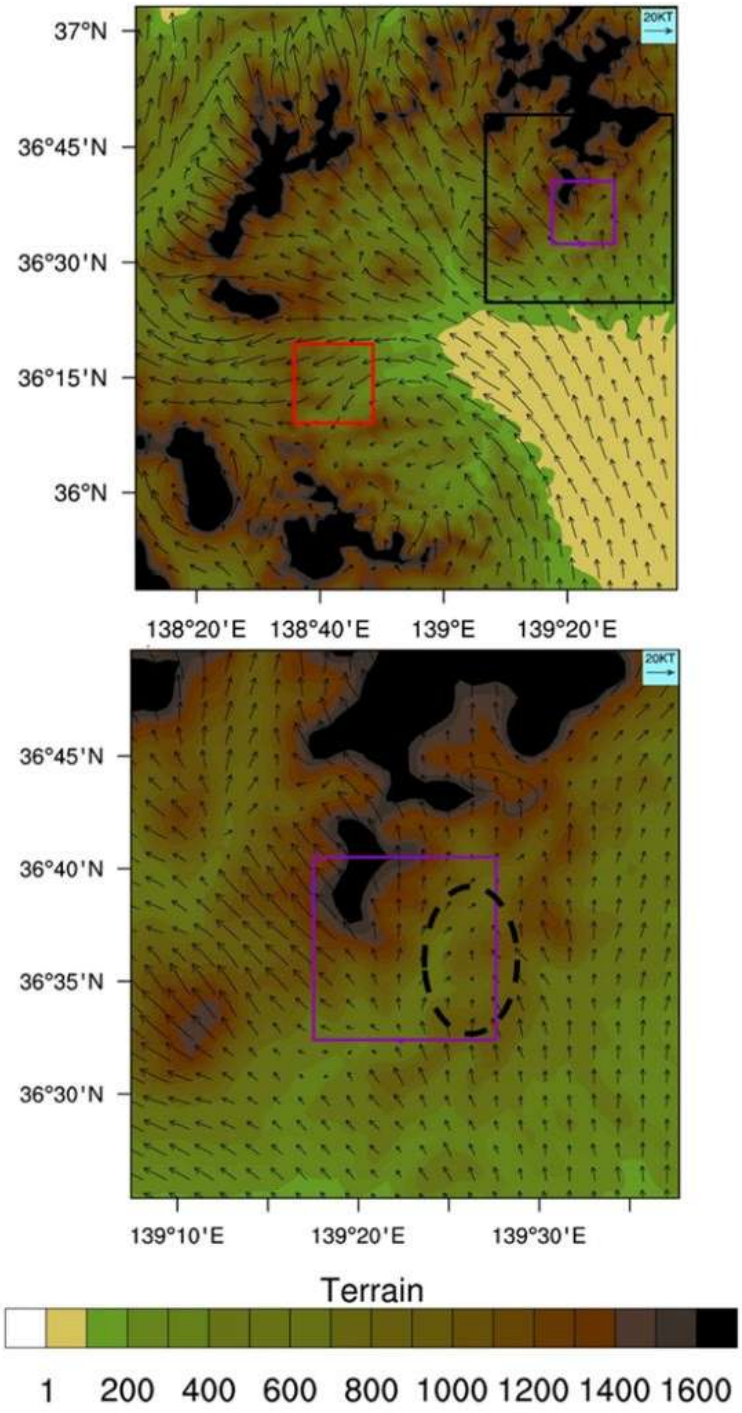

Figure 9. The distribution of surface wind at 16:10 JST on 16 June, 2016 in the control case. The figure below is an enlarged view of the black frame in the above figure. The red and purple squares show the seeding and the catchment area, respectively. The area surrounded by a black broken line shows the notified convergent area.

km again at 70 min (Figure 12f). The increase in the mass mixing ratio of cloud water and the ascent of the cloud top in the period from 30 to 50 min after seeding seem to correspond with the ascending flow in this area. There is always an ascending flow of 1.0 m s^{-1} around 139.4°E in a layer between heights of 1 and 2 km and the cloud water is generated there. The ascending flow is formed by the convergence shown in Figure 9 and this

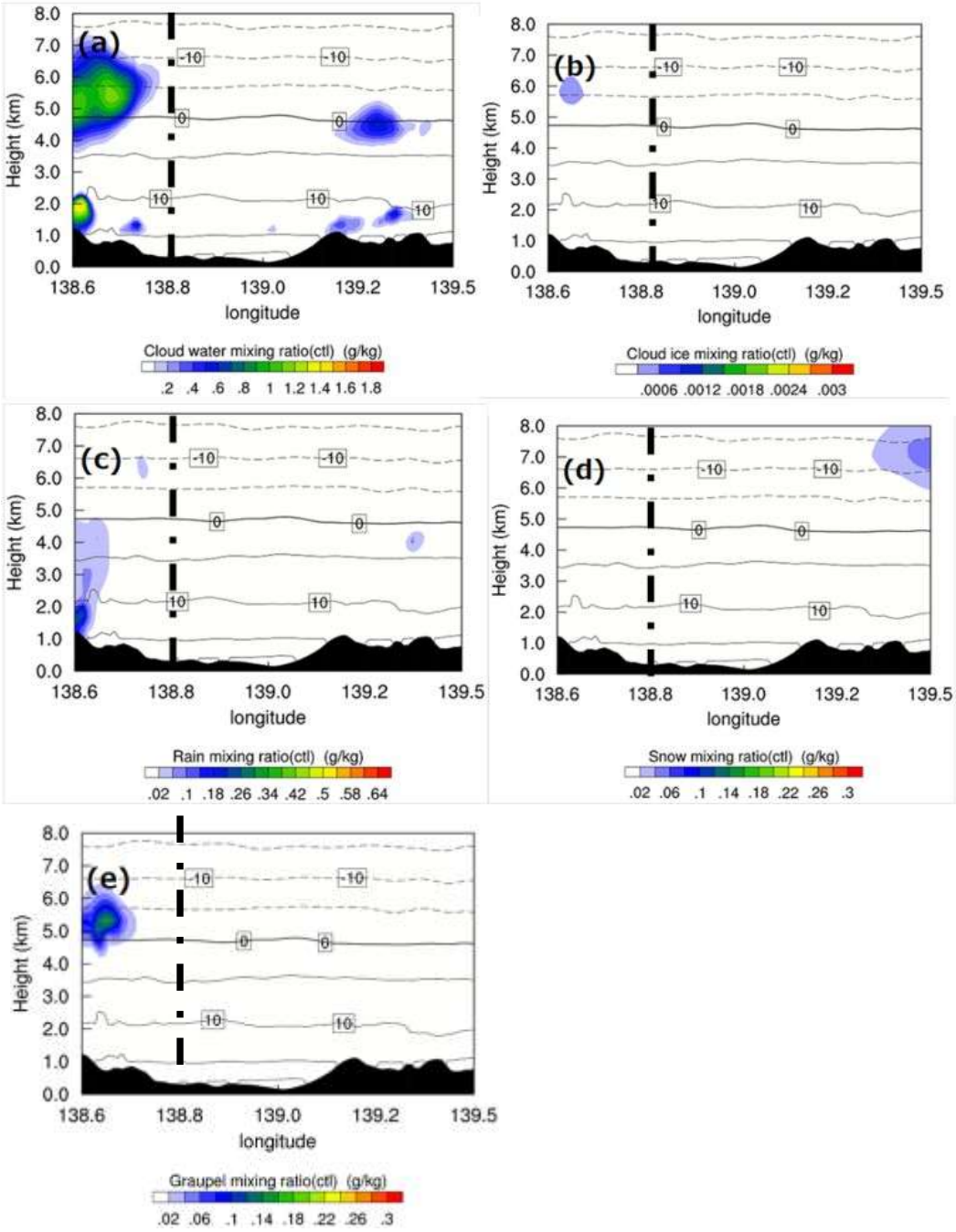

Figure 10. The distributions of mass mixing ratio of five hydrometeor species at the seeding time (16:10 JST) in cross-sections on line 1 in Figure 2. The five species are (a) cloud water, (b) cloud ice, (c) rain, (d) snow, and (e) graupel. Atmospheric temperature (°C) is presented by solid (positive) and broken (negative) lines in the figures. The dash-dotted lines in the figures show the eastern edge of the seeding area.

convergence is supposed to be due to topographical effects.

To understand the mechanisms that result in the maximum in the accumulated precipitation amount in the eastern part of the catchment area in Figure 2, the distributions of the cloud water mass mixing ratio, rain mass mixing ratio, and magnitude of the updraft at 64, 67 and 76 min after the simulated seeding are shown in Figure 13. These cross-sections are taken along the line indicating cross-section 2 in Figure 2. There is an ascending flow of 1.0 ms^{-1} between longitudes of 139.4°E and 139.5°E in a layer between heights of 1.5

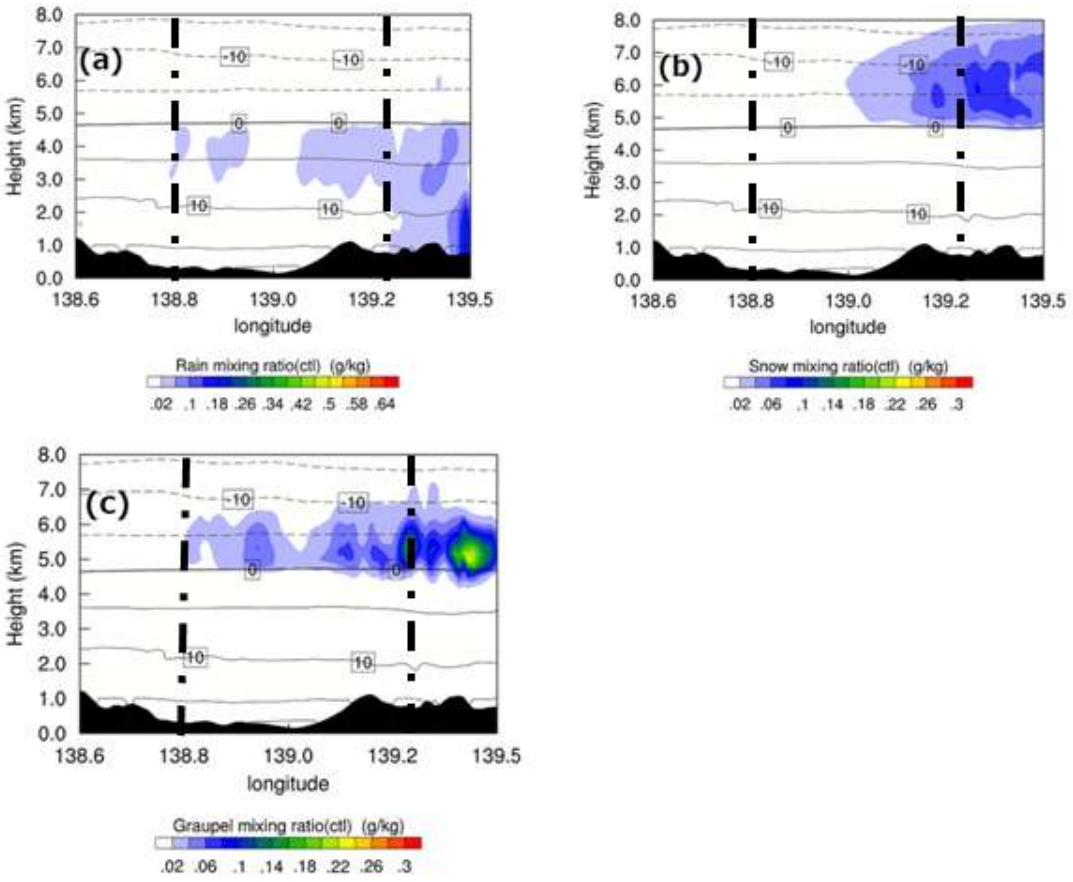

Figure 11. Same as Figure 10, but for (a) rain, (b) snow, and (c) graupel at 90 min after seeding (17:20 JST). Dash-dotted lines in the figures show eastern edge of the seeding area and western edge of the catchment area.

and 2.5 km at 64 min in Figure 13c. The updraft is supposed to be due to the topographical effects as mentioned above. Corresponding to the updraft, there is an area of cloud water mixing ratio of 1.5 g kg^{-1} in a layer between heights of 1.0 and 3.0 km in Figure 13a, and an area where the rain mixing ratio extends to the ground surface from the cloud in Figure 13b. At 67 min, the ascending flow area becomes narrower, the cloud water mixing ratio decreases, and the corresponding area showing the rain mixing ratio becomes narrower, too. An area including the rain mixing ratio in the upper levels between heights of 2.0 and 5.0 km connects to the lower area of the rain mixing ratio described above at the time indicated in Figure 13e. At 76 min, the rain mixing ratio increases in the area of interest below 2 km height (Figure 13h) though the cloud water mixing ratio decreases by 0.4 g kg^{-1}. Therefore, the increase in the rain mixing ratio there is likely due to rain from the upper cloud.

CLOUD EVOLUTION WITH WEAK SEEDING

In the weak seeding case, a seeding agent comparable to 1 kg of dry ice is injected into the cloud over the seeding area. The seeding is estimated to generate ice crystals whose number density is 1.15 × 10^5 kg^{-1}, following the estimates in section 3. The cloud water mixing ratio is estimated to have decreased by 0.75 g kg^{-1} to grow the ice crystals to generate drizzle particles with a diameter of 0.5 mm. Then, the weak seeding is expected to significantly influence the seeded cloud which has a cloud water mass mixing ratio of around 1 g kg^{-1}, such as shown in Figure 10a. Results from the weak seeding are shown below. The difference in the accumulated precipitation amount between the weak seeding and the no seeding cases (seed – control) (Figure 2) is shown in Figure 14. The cumulative precipitation is measured over 90 min from 16:10 JST to 17:40 JST. The accumulated precipitation amount increases near the seeding area and over an area from 139.0°E to the catchment area. A significant increase of 0.4 mm on the eastern part of the catchment area is seen, where the maximum precipitation amount is 2.7 mm in the control case (Figure 2).

The increase in the accumulated precipitation from the weak seeding is analyzed hereafter. Differences in the mass mixing ratio between the weak seeding and the

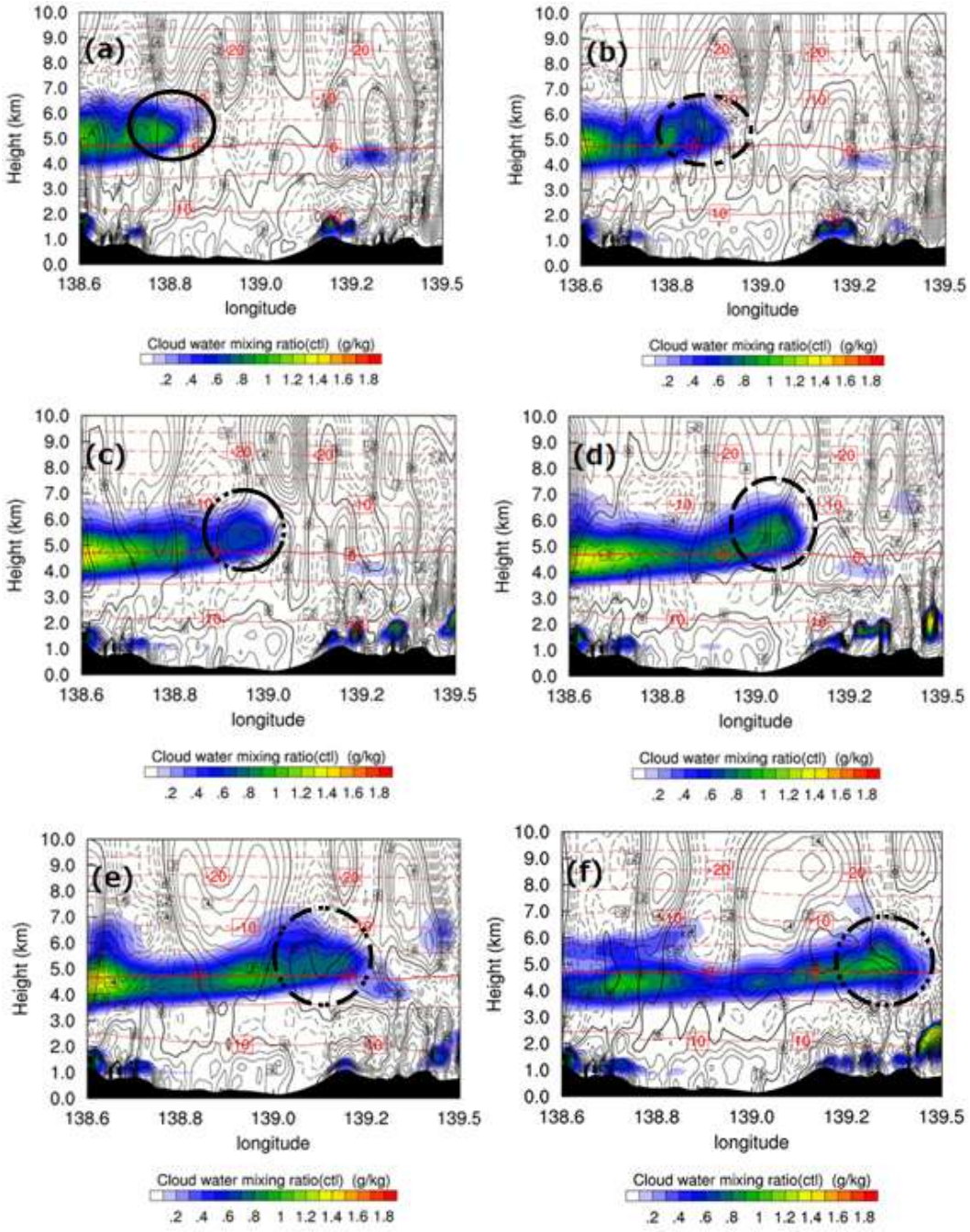

Figure 12. Same as Figure 10, but for cloud water mass mixing ratio and vertical wind component at (a) 10, (b) 20, (c) 30, (d) 40, (e) 50, and (f) 70 minutes after seeding. Eastern tip of the cloud surrounded by a broken line is the part assumed to be seeded. Atmospheric temperature is presented by red solid (for positive temperature) and broken (for negative temperature) lines in the figure. The black solid (ascend) and broken (descend) lines show contour of vertical wind speed by 0.1 m s^{-1} intervals.

control cases of five hydrometeor species 30 minutes after the seeding time (16:40 JST) are shown in Figure 15. The five species are cloud water, snow, cloud ice, graupel, and rain. The eastern edges of the seeding area are shown by dash-dotted lines in the figures. The cloud ice mass mixing ratio (Figure 15c) increases by 0.002 g kg^{-1} due to the seeding and it is more than 3 times larger than that in the control case in Figure 10b. The increase in the cloud ice mass mixing ratio due to the simulated seeding at the initial instance was only 6.49×10^{-6} g kg^{-1} based on the estimates in the section of numerical model, therefore the cloud ice mass mixing ratio in

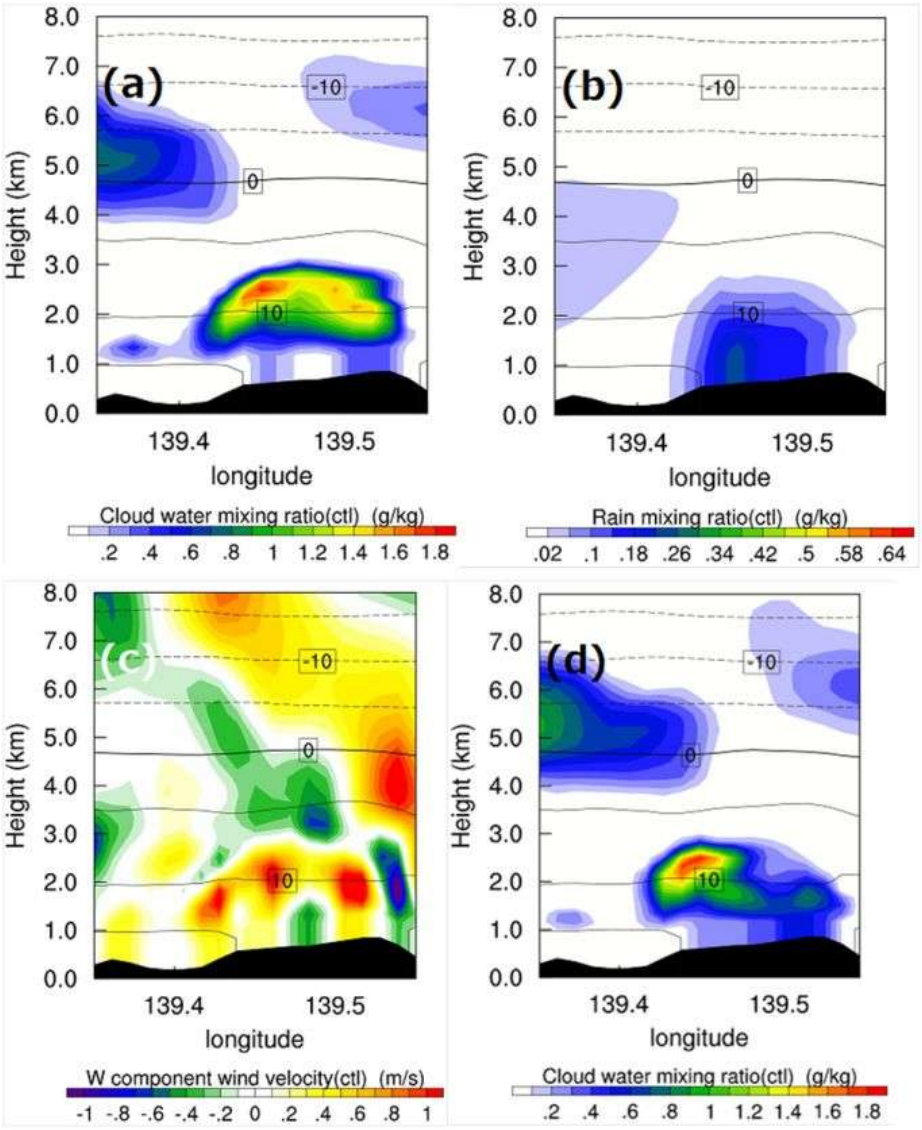

Figure 13. Distributions of (a, d, g) cloud water mass mixing ratio, (b, e, h) rain mass mixing ratio, and (c, f, i) magnitude of updraft at (a, b, c) 64, (d, e, f) 67, and (g, h, i) 76 min after the assumed seeding time. These cross-sections are on the line for cross-section 2 in Figure 2. Solid (positive) and broken (negative) lines in the figures show isotherms at 5°C intervals.

Figure 15c is believed to be the result of a rapid growing of the cloud ice after seeding, through processes such as deposition of water vapor on the cloud ice particles. The mass mixing ratios of snow and graupel are increased by up to 0.18 and 0.18 g kg^{-1} as shown in Figure 15b and d. The snow particles are generated through an auto-conversion process from cloud ice, and grow through the deposition and collection of cloud ice and cloud water as described in the Milbrandt scheme. The graupel particles are generated through another auto-conversion process from snow and cloud ice, and grow through the deposition and collection of cloud water and ice. Some updraft is generated in the area with an increased snow mixing ratio and above the area experiencing released latent heat from freezing. The maximum decrease of the mass mixing ratio of cloud water is 0.40 g kg^{-1} (Figure 15a), and the decrease is due to the conversion required to increase the snow, graupel, and rain mass mixing ratio. The maximum increase in the rain mixing ratio is 0.10 g kg^{-1} (Figure 15e), and seems to be due to melted snow and graupel particles near the 0°C level of atmospheric temperature because the area of snow increase between 138.85°E and 139.05°E corresponds well with the increase in the rain mixing ratio and the position of the maximum of the rain mass mixing ratio increase corresponds well with that of the maximum

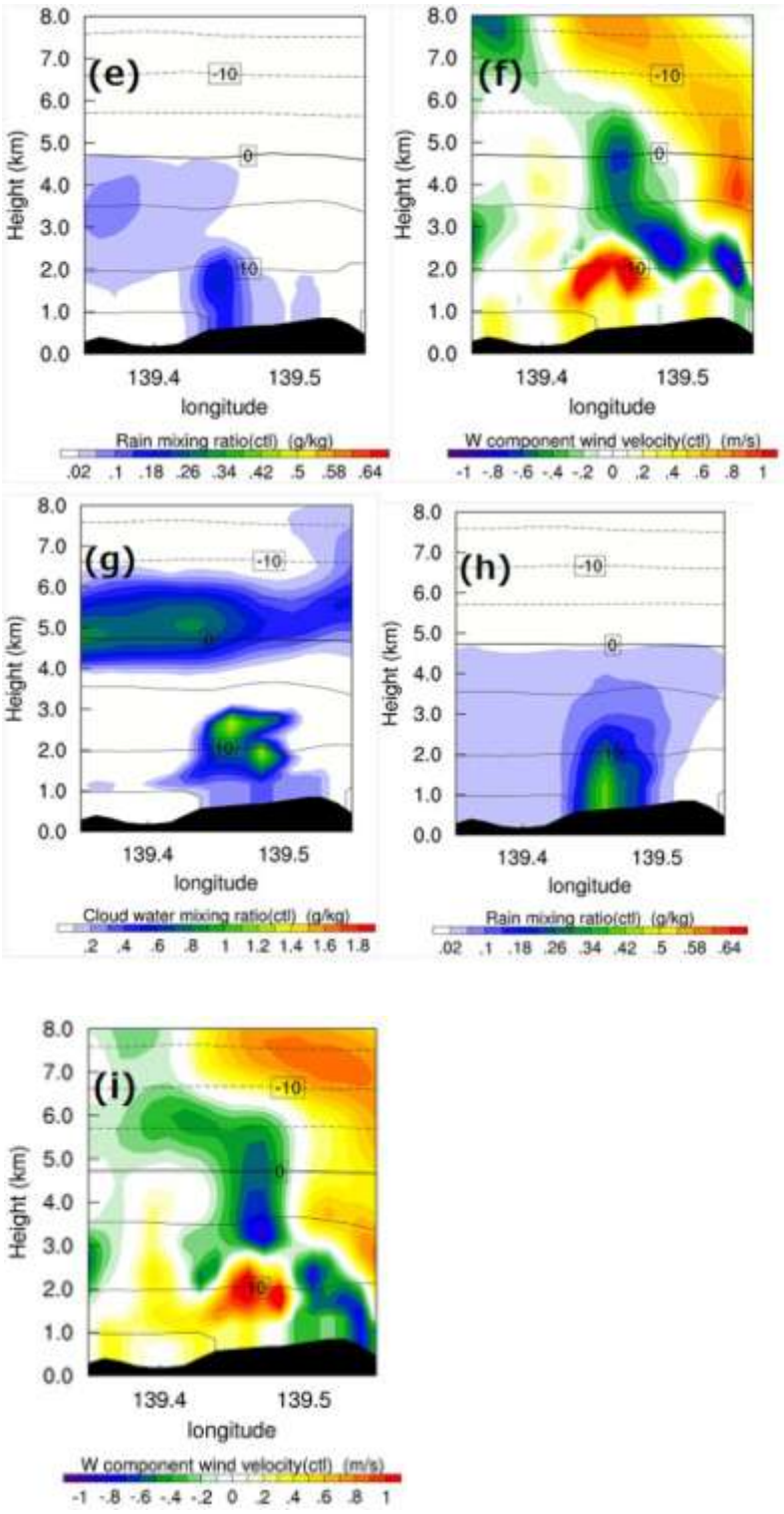

Figure 13. Continues.

increase of the graupel mass mixing ratio.

Differences in the mass mixing ratios of the five hydrometeor species 70 min after seeding (17:20 JST) are shown in Figure 16. The catchment area is between 139.3°E and 139.5°E in the cross-sections and the western edge of the study area is shown by dash-dotted

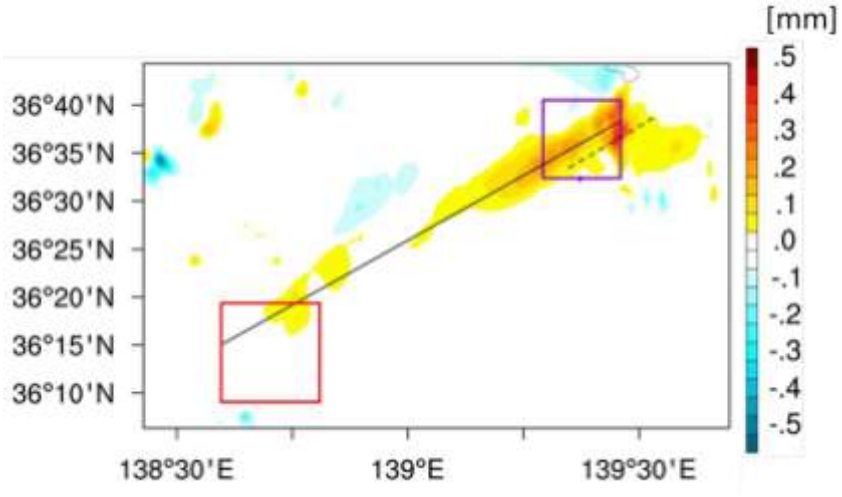

Figure 14. Same as Figure 2, except for difference of accumulated precipitation amount between the weak seeding and no seeded (the control) cases. The accumulated period is 90 min from 16:10 to 17:40 JSTs.

lines in the figures. The maximum increase in the cloud ice mass mixing ratio decreases to 0.0012 g kg^{-1} (Figure 16c). This decrease suggests that most cloud ice particles have been collected by or converted to snow and graupel particles. The maximum of the mass mixing ratio of the cloud water decrease is 0.40 g kg^{-1} and is the same as 30 min after seeding though the area is wider (Figures 15a and 16a). The maximum of the increase in the snow mixing ratio rises from 0.18 to 0.24 g kg^{-1} during this period (Figures 15b and 16b) and the updraft in and above the increased snow mixing ratio area is strengthened in this period, too. The maximum of the graupel mixing ratio increase shows a small decrease from 0.18 to 0.15 g kg^{-1} (Figures 15d and 16d). The maximum difference in the rain mixing ratio decreases from 0.10 to 0.07 g kg^{-1} just below the level of 0°C (Figures 15e and 16e). The increase in the rain mass mixing ratio is due to melted snow and graupel, as before, though the increase in area is wider near the ground at 70 min after seeding than that at 30 min Additionally, it should be noted that the distribution of the rain mass mixing ratio increase has one more maximum near a height of 1 km (Figure 16e). This maximum relates to a significant increase of the accumulated precipitation amount on the eastern part of the catchment area shown in Figure 14 and is investigated in detail later.

To clarify the role of the vertical components of the difference in wind, the distribution of the difference in total mass mixing ratio of liquid and solid water is shown in Figure 16f. The difference in total mass mixing ratio is defined as the sum of the cloud water, snow, cloud ice, graupel, and rain difference in mass mixing ratio between the weakly seeded cloud and the cloud in the control case. The increase of the total mass mixing ratio near 139.5°E is due to the increase in the snow mixing ratio (Figure 16b). Furthermore, at this location, the snow is not converted from pre-existing cloud water, because the difference in the total mass mixing ratio is positive as shown in Figure 16f. The increase in the total mass mixing ratio means that the ascending flow caused by the seeding generates new snow particles. The decrease in the total mass mixing ratio over 139.3°E is due to the decrease in cloud water (Figure 16a). The cloud water mass mixing ratio at this location is decreased and converted into snow which descends as rain and evaporation in the downward flow. Then, the weak seeding enhances the snow generation in the ascending flow area but this generation is not great because the area of increase is narrow as shown in Figure 16f.

Differences in the mass mixing ratio of cloud water and rain 76 min after seeding (17:26 JST) are shown in Figure 17. These cross-sections are taken along the line for cross-section 2 in Figure 2. In the control case, the rain mass mixing ratio from heights of 2.0 and 5.0 km are connected to the lower area of rain mass mixing ratio at 17:17 JST as shown in Figure 13e, as described before. In the weakly seeded case, they are connected at 17:17 JST, also, and the difference in the rain mass mixing ratio is increased by 0.12 g kg^{-1} between 139.4°E and 139.5°E below 2 km height to form the local maximum area in this study as shown in Figure 17b. The mass mixing ratio of cloud water decreases by 0.1 g kg^{-1} in this same area between heights of 1.5 and 3.0 km (Figure 17a). These results suggest that the increase in the rain mass mixing ratio by the seeding affects the underlying cloud to form a local maximum of the difference in the rain mass mixing ratio below. The results also show the effectiveness of glaciogenic seeding conducted in a relatively warm cloud which has a super-cooled portion near the top. In this case, it is supposed that the increased precipitation

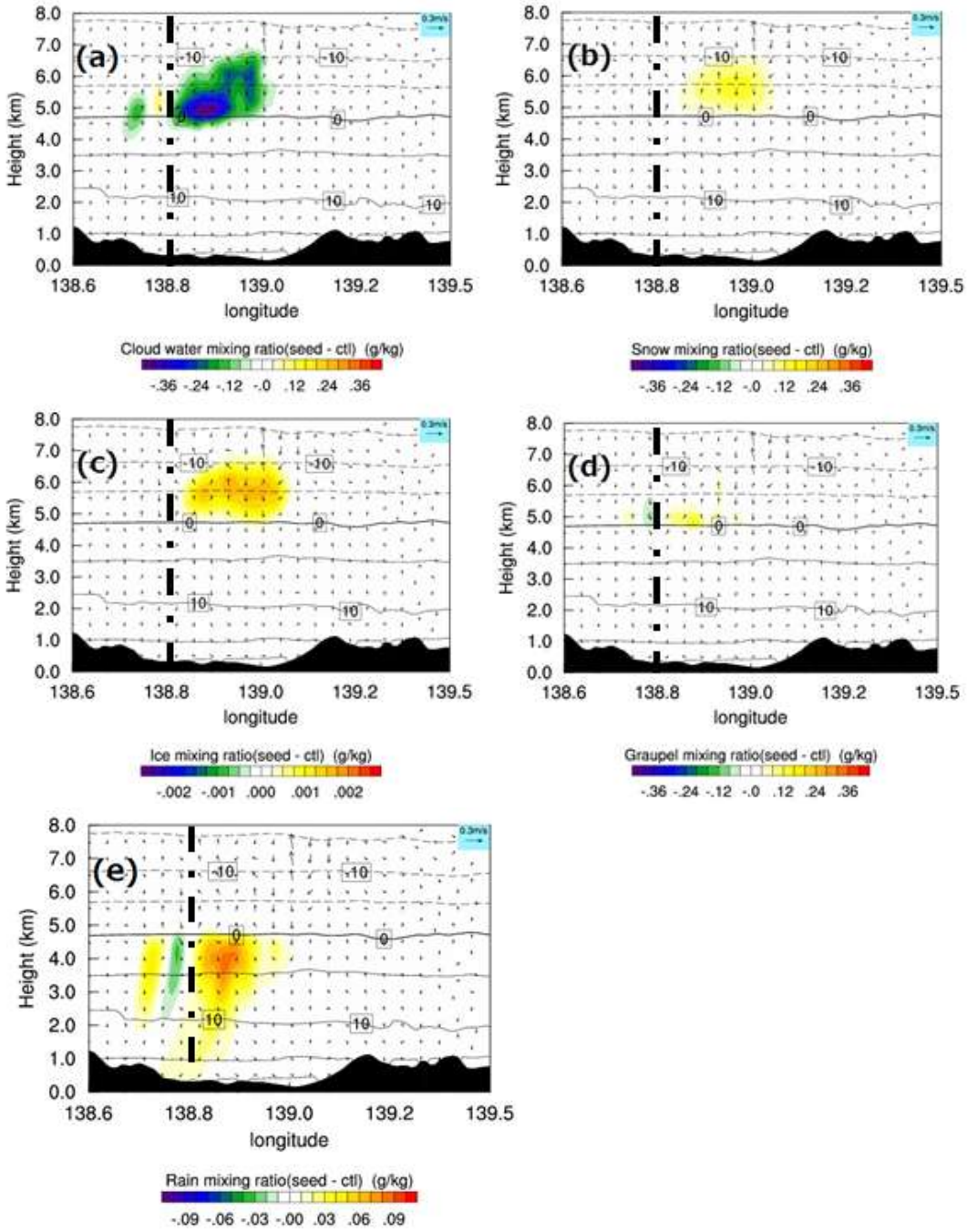

Figure 15. Same as Figure 10, but for differences in mass mixing ratio of the five hydrometeor species between the weak seeding and the control cases at 30 min after the seeding time (16:40 JST). The five species are (a) cloud water, (b) snow, (c) cloud ice, (d) graupel, and (e) rain. Arrows in the figures show differences in winds between the weakly seeded and the control cases.

amount by the glaciogenic seeding conducted on the super-cooled portion of the cloud will be more effective while the raindrops are falling through the warmer lower portion of the cloud.

In summary, the increase of the precipitation amount after seeding is caused by the increase in the snow and graupel mixing ratio, and the effects of the snow increase are larger near the catchment area than near the seeding area. Incidentally, the cloud water mass mixing ratio of less than 0.6 g kg^{-1}, which is about half of that in the control case, is still observed 70 min after seeding. Therefore, increasing the amount of seeding agent is expected to increase the amount of precipitation. The effects of the ordinary seeding method, which uses 15

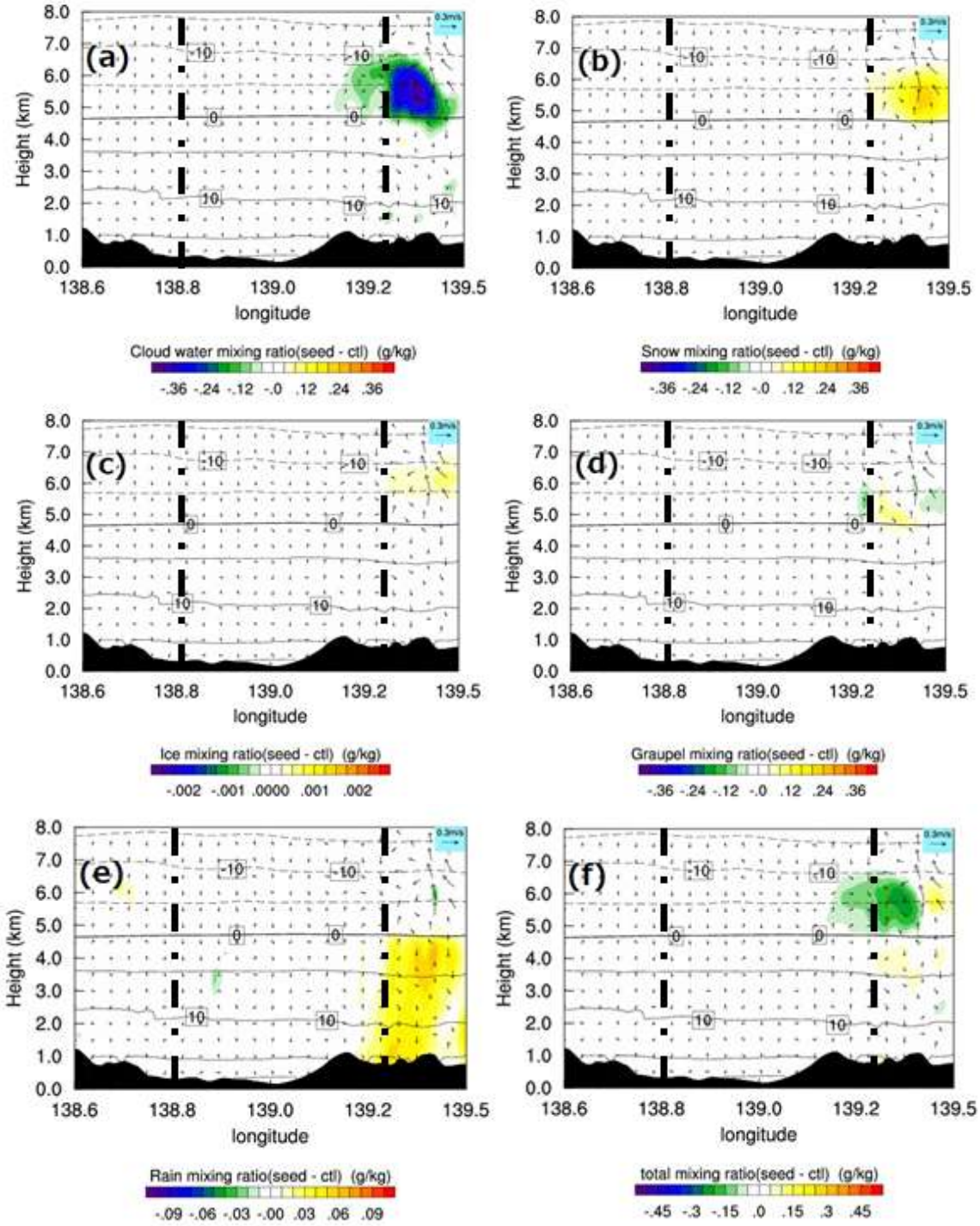

Figure 16. Same as Figure 15, but for differences at 70 min after seeding (17:20 JST). Figure 16f shows distribution of sum of difference in water mass mixing ratio without water vapor. The sum is for cloud water, snow, cloud ice, graupel, and rain differences in mass mixing ratio.

times more seeding agent than the weak seeding, and the multiple seeding method of 15 individual seedings at 5-min intervals, while tracking the cloud, are investigated in the next section.

CLOUD EVOLUTION WITH ORDINARY SEEDING METHOD

In the ordinary cloud seeding method, 15 times more

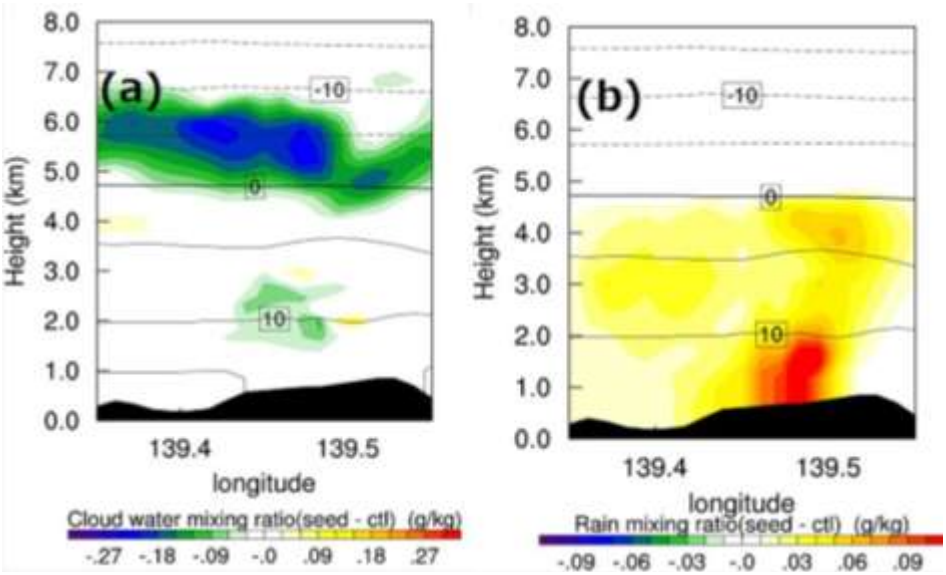

Figure 17. Differences in the mass mixing ratio of cloud water and rain between the weakly seeded cloud and the cloud in the control case at 76 minutes after seeding (17:26 JST). (a) Cloud water and (b) rain. These cross-sections are taken along the line for cross-section 2 in Figure 2. Solid and broken lines in the figures are isotherm at 5°C interval.

seeding agent is injected into the cloud than in the weak seeding method, as described in the previous section. The increase in the accumulated precipitation amount over 90 min in the ordinary seeding method is presented in Figure 18. Compared with the control case (Figure 2), a significant increase of 0.6 mm is observed near the eastern edge of the catchment area, where an accumulated precipitation of 3.0 mm is observed in the control case and the increase is 0.4 mm in the weakly seeded case (Figure 14). Furthermore, the increase occurs just beyond the seeding area in the ordinary seeding case (Figure 18), while it occurs beyond of 139°5′ E on the line showing the cross-section position in the weakly seeded case. A slight decrease in the accumulated precipitation is observed in areas near the increase.

The distribution of the cloud water mass mixing ratio 30 min after seeding is presented in Figure 19a. Compared with the control case (Figure 12c), the cloud water has largely disappeared between 138.8°E and 139.0°E, and between heights of 5.5 and 6.5 km, where a cloud water mixing ratio of 0.6 g kg^{-1} is observed in the control case (Figure 12c). A thin cloud layer remains between heights of 4 and 5.5 km (from the 3 to −4°C levels of atmospheric temperature) under the area where the cloud has dispersed. The thin cloud has a maximum cloud water mass mixing ratio of only 0.4 g kg^{-1}. In the area where the cloud water disappeared, a snow mass mixing ratio increase of 0.6 g kg^{-1}, cloud ice mass mixing ratio increase of 0.03 g kg^{-1}, and temperature increase of 0.45°C are observed (Figure 19b, c, f). The cloud ice mass mixing ratio increased during the first 10 min and then decreased gradually. The maximums of the snow mass mixing ratio increase and temperature increase are observed at heights of 5.2 and 6.2 km, respectively. The top of the warming area is near the −10°C level of the atmospheric temperature which is at the cloud top height in the control case (Figure 12c). A maximum of the upward flow caused by the warming is observed near the top of the warmed air parcel and the upward flow is formed until at least a height of 9 km. The upward flow over the cloud top causes a cooling of the atmosphere up to a height of 10 km through adiabatic ascending without the release of latent heat from the cloud. The ascending flow influenced by the released latent heat forms a downward flow over the lee side of the increased snow area at 139.05°E and over the windward side at 138.8°E (Figure 19b). Both of the descending flows form a convergent area in the increased snow mixing ratio area which supports the ascending flow. The rain mass mixing ratio increases by 0.1 g kg^{-1} below the area of the increased snow mass mixing ratio in Figure 19e and the mass mixing ratio is about three times larger than that in the control case. However, the precipitation amount does not increase as much there, because it is so low in the control case. The magnitude of the snow mass mixing ratio increase in the ordinarily seeded cloud is about 3 times larger than that in the weakly seeded cloud. These results suggest that using more of the glaciogenic seeding agent is ineffective in a cloud where most of the cloud water has been sublimated out to generate snow particles due to the seeding. The graupel mass mixing ratio decreases everywhere (Figure 19d), but remains reasonably high.

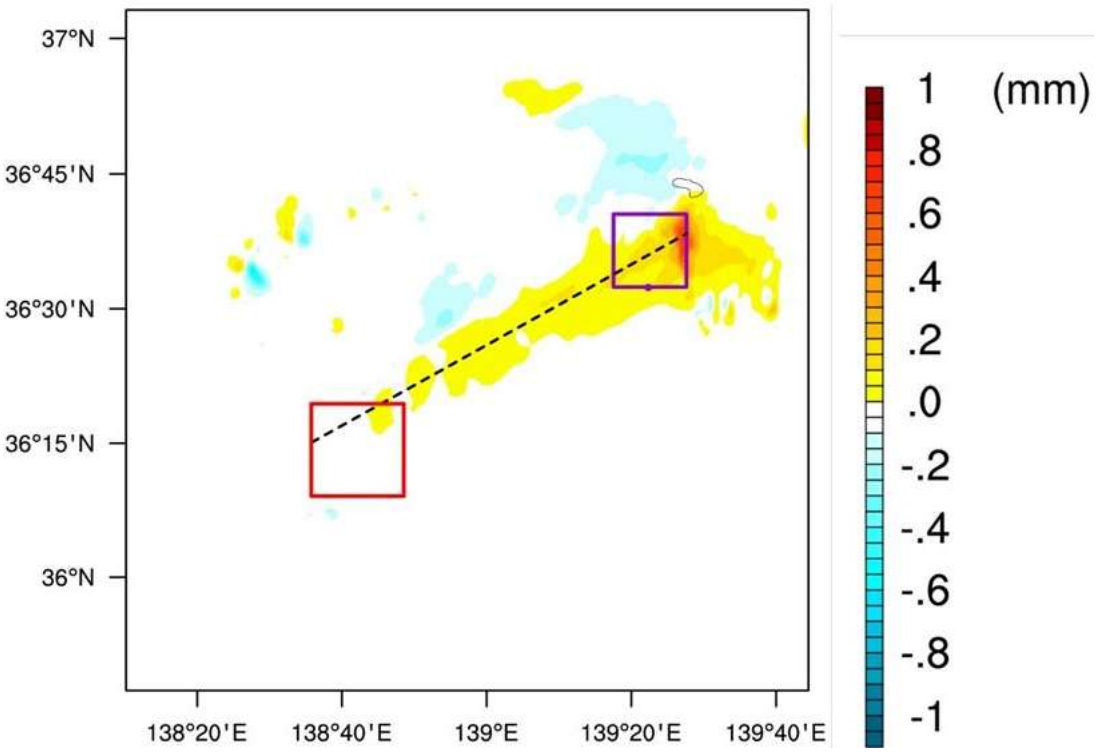

Figure 18. Same as Figure 14, but for accumulated precipitation amount in the ordinary seeded case. Broken line in the figure shows a position of the cross-section 1.

The distribution of the cloud water mass mixing ratio 70 minutes after the ordinary seeding is presented in Figure 20a. The seeded cloud part is located between 139.3°E and 139.5°E at this time. The cloud top height of the seeded part is nearly 6.0 km and higher than that at 30 min after the seeding by 0.5 km (Figure 19a) and the maximum of the cloud water mass mixing ratio increases from 0.4 g kg^{-1} (Figure 19a) to 0.8 g kg^{-1} at this time (Figure 20a) at 139.3°E. The maximum of the differences in snow mass mixing ratio of 0.5 g kg^{-1} is located at 139.4°E (Figure 20b) and the maximum of the differences decreases from that at 30 min after seeding (Figure 19b). The magnitude of the snow mass mixing ratio increase is small near the maximum of the cloud water at 139.3°E. The increased snow mass mixing area seems to be slightly separated from the cloud water area. In the weakly seeded cloud, the position of the maximum of the snow mass mixing ratio increase is the same as that in the ordinarily seeded cloud but the cloud water distribution is elongated slightly further eastward than that in the ordinarily seeded cloud (Figures 21, 16b, 20a, b). Therefore, the increased snow mass mixing ratio area in the weakly seeded cloud does not appear to be separated from the cloud water area so much as that in the ordinarily seeded cloud. The distribution of the differences in cloud ice mixing ratio is shown in Figure 20c. The mixing ratio is less than 0.01 g kg^{-1} and the area of increased cloud ice seems to move with the increased snow mixing ratio. The distributions of the snow and cloud ice mass mixing ratios are unlikely to affect the central part of the cloud water mixing ratio at 139.3°E. The ascending flow is forced by the released latent heat from freezing due to the seeding as described above (Figure 20f). The maximum warming of the atmospheric temperature is 0.5°C at 139.4°E. The graupel mass mixing ratio decreases (Figure 20d), and thus the increase of the rain mass mixing ratio is due to the increase of the snow mass mixing ratio (Figure 20e). The distribution of the differences in total mass mixing ratio of liquid and solid water at 17:20 JST is shown in Figure 22a. The increase and decrease of the total mass mixing ratio are due to the snow mass mixing ratio increase (Figure 20b) and the decrease of cloud water (Figure 22b) as in the weakly seeded cloud. The magnitude of the increase of the total mass mixing ratio in this case is larger than that in the weakly seeded case owing to the stronger ascending flow. Then, the ordinary seeding seems to enhance snow generation in the ascending flow area and weakens the surrounding clouds by converting the cloud water to snow which falls rapidly or evaporates in the downward flow area.

EVOLUTION OF THE MULTIPLY SEEDED CLOUD

As described above, ordinary seeding can increase the

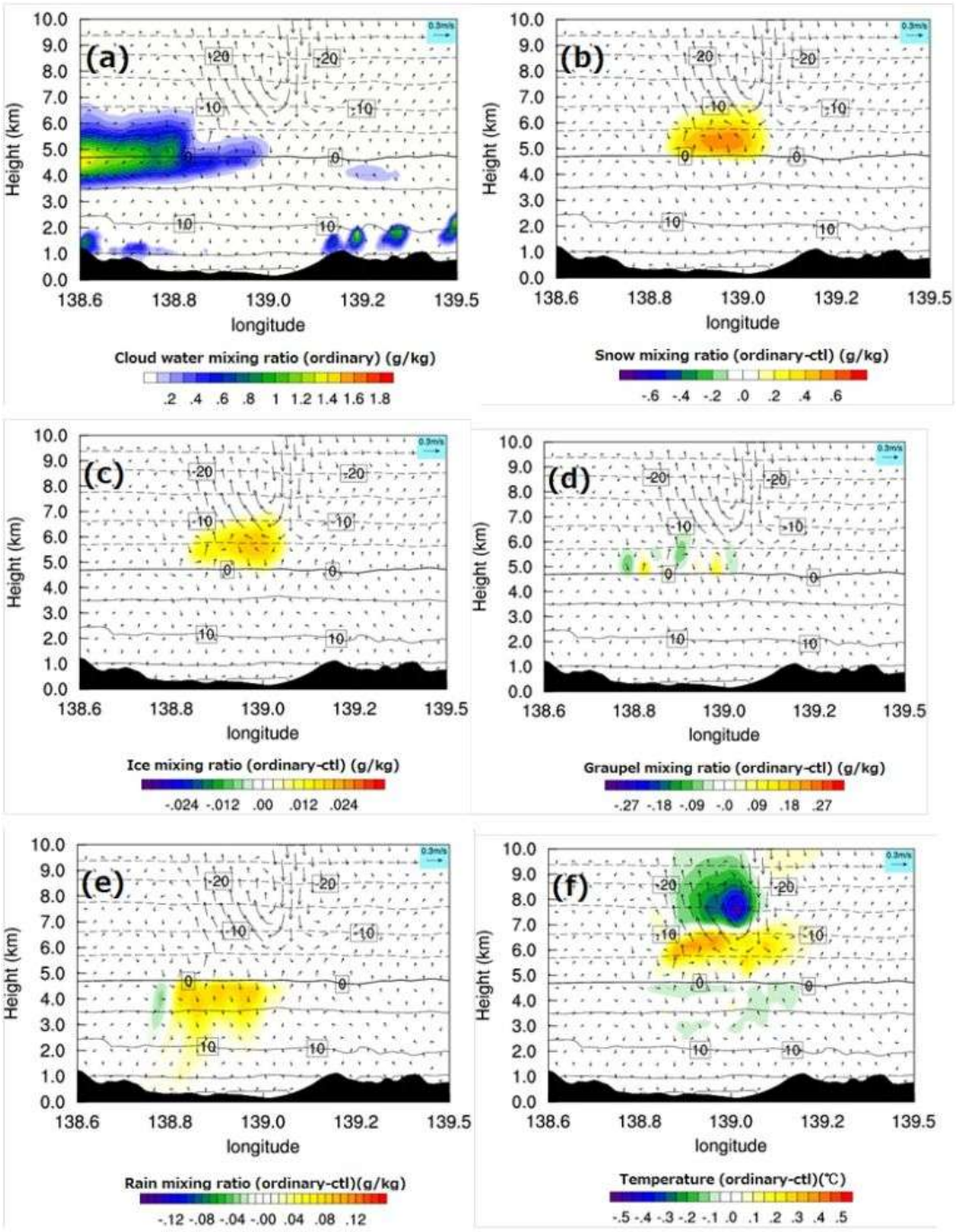

Figure 19. Same as Figure 15, but for mass mixing ratio of (a) cloud water, differences in mass mixing ratio of (b) snow, (c) cloud ice, (d) graupel, and (e) rain, and (f) differences in temperature in the cross section at 30 min after seeding.

total amount of precipitation. On the other hand, the increased areas of the snow mass mixing ratio and cloud ice mixing ratio are slightly separated from the area with a large cloud water mass mixing ratio and these conditions are not adequate for snow and cloud ice particles generated through the seeding to work on cloud water effectively. These facts suggest that the total precipitation can be increased by converting the remaining cloud water into snow with more glaciogenic seeding. For this reason, a multiple seeding method is tested to enhance precipitation in the catchment area. In this method, a seeding agent comparable to 1 kg of dry

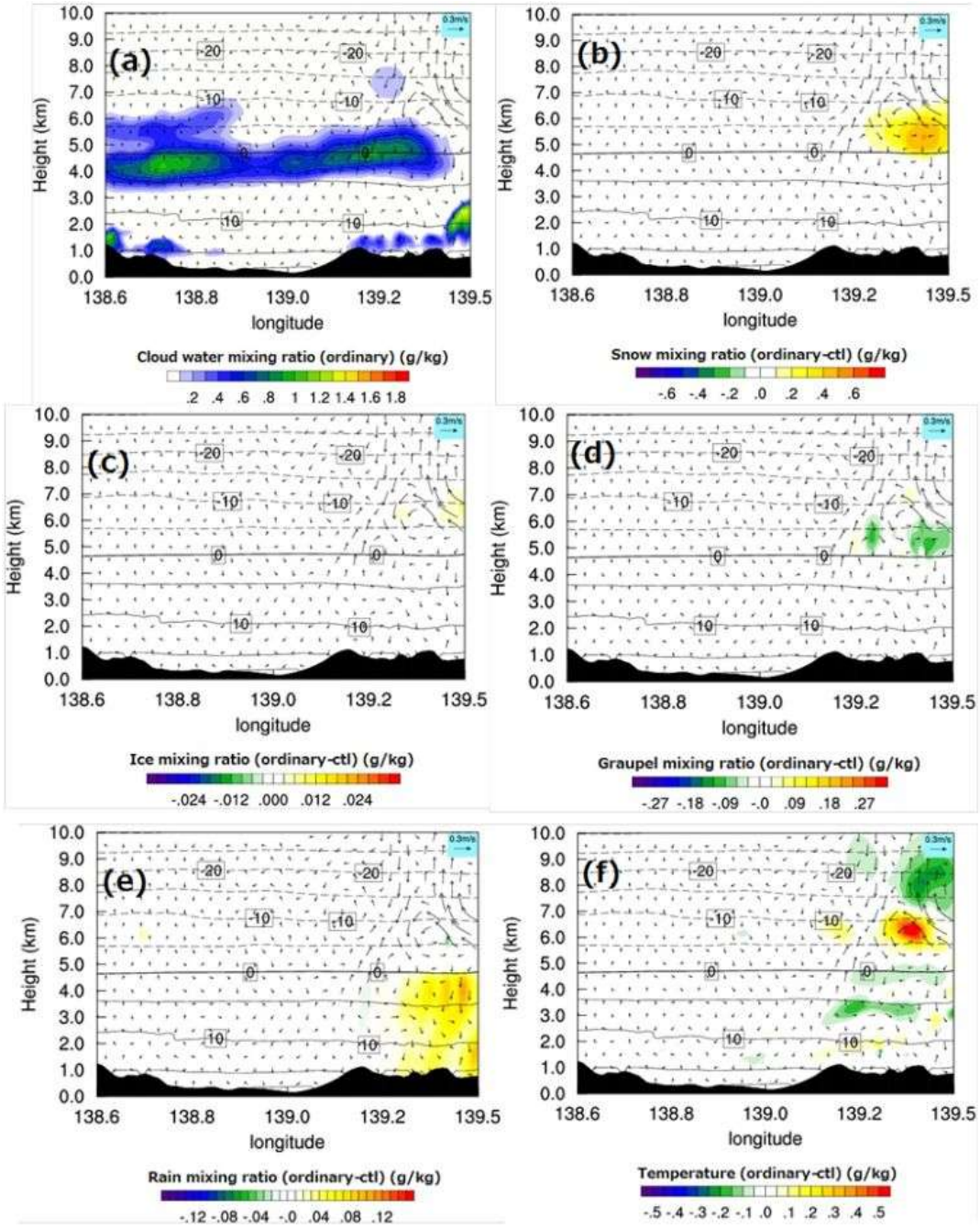

Figure 20. Same as Figure 19, but for 70 min after seeding.

ice is injected at 5-min intervals while tracking the seeded cloud, as described above.

The increase in the total precipitation over 90 min for the multiply seeded cloud is presented in Figure 23. Comparing this with the ordinarily seeded case, the accumulated precipitation over the catchment area is 0.06 mm greater than in the ordinarily seeded case, while the total amount of seeded agent is the same in both cases. The distributions of the accumulated precipitation are similar. The eastern edge of the catchment area shows the largest increase in precipitation in both cases.

The distribution of the cloud water mass mixing ratio 30 min after the beginning of the multiple seeding is shown in Figure 24a. The cloud water mass mixing ratio of 0.5 g kg^{-1} is also observed at 5.5 km above 138.85°E where the narrower region of the cloud water mass mixing ratio is observed in the cloud with ordinary seeding (Figure 19a). The cloud top height is 6.2 km there, which is

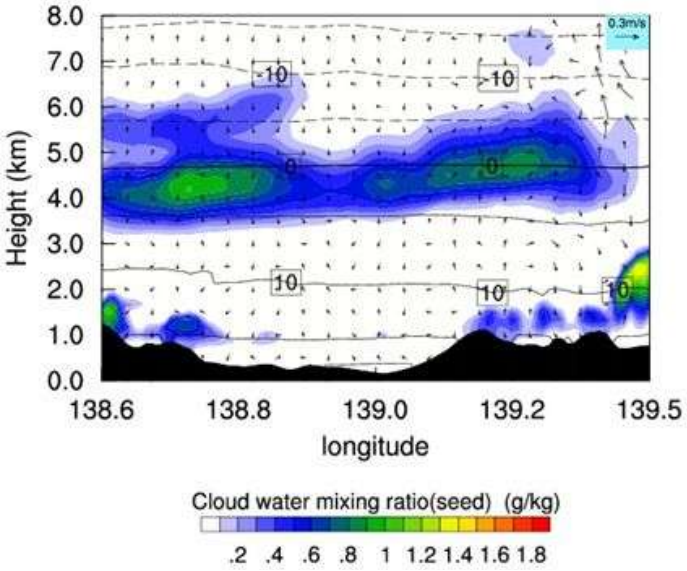

Figure 21. Distribution of cloud water mixing ratio at 70 min after the weak seeding.

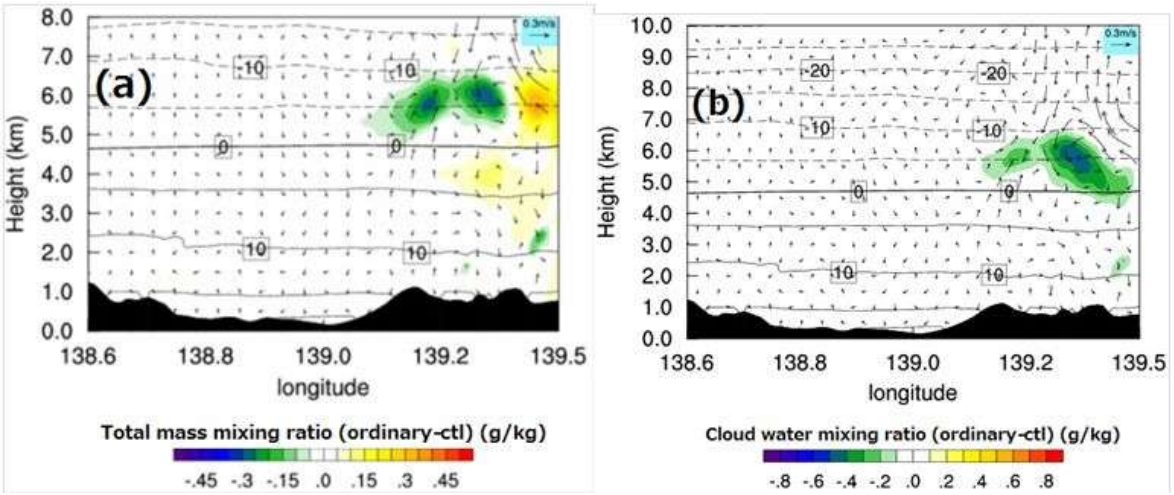

Figure 22. (a) Differences in total amount of solid and liquid hydrometeor species' mass mixing ratio and (b) distribution of differences in cloud water mass mixing ratio in the ordinarily seeded cloud at 70 min after seeding (17:20 JST).

slightly higher than for the ordinarily seeded cloud (5.5 km, Figure 19a). These results show that the seeding amount is insufficient in the multiply seeded cloud in comparison with the ordinarily seeded cloud. The effects of insufficient seeding agent are observed in the distributions of the snow and cloud ice mass mixing ratio increase and the degree of atmospheric temperature change (Figures 19b, c, f, 24b, c, f). The increase in the snow and cloud ice mass mixing ratio in the ordinarily seeded cloud are 3 times and 1.4 times larger than those in the multiply seeded cloud, respectively. The distribution of the differences in wind shows an ascending flow from the increased snow area and a compensating downward flow on both sides of the updraft in the ordinarily seeded cloud (Figure 19b), while the differences in winds are not so organized in the multiply seeded cloud (Figure 24b). The magnitude of the atmospheric temperature change due to multiple seeding is less than that in the ordinarily seeded cloud. However, the maximum rain mass mixing ratio increase under the multiply seeded cloud is larger than that under the ordinarily seeded cloud (Figures 19e and 24e). The difference between the distributions of the rain mass mixing ratios in the multiply and ordinarily seeded clouds

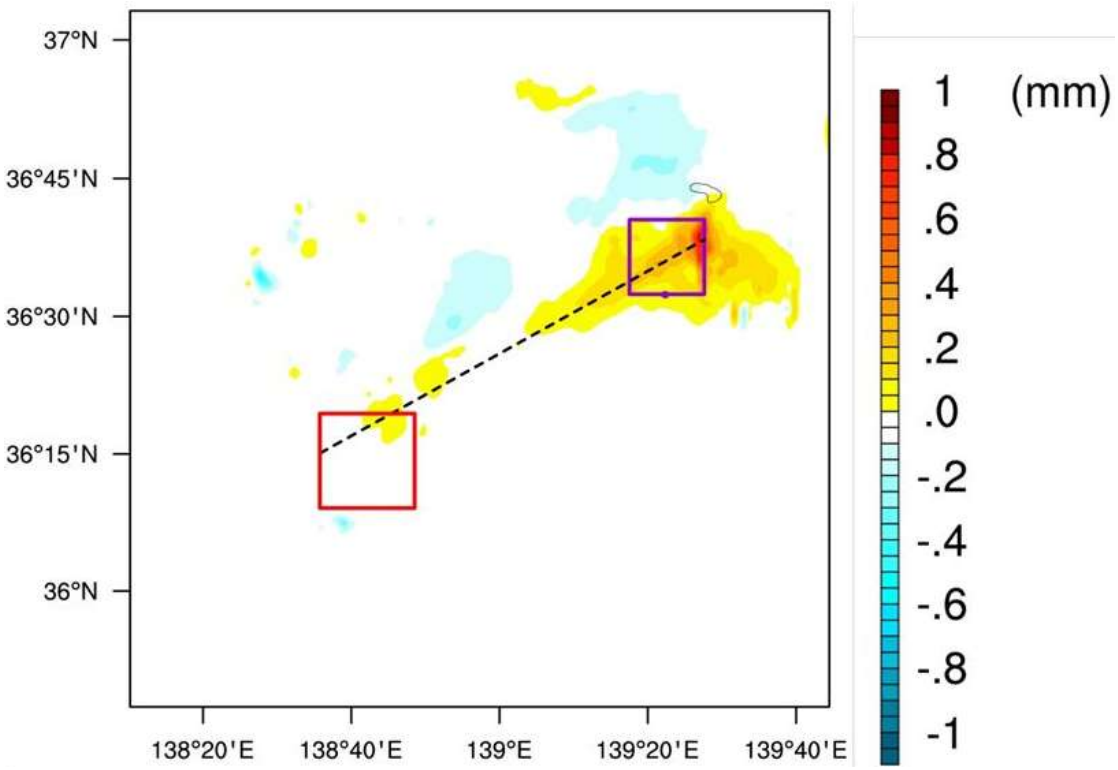

Figure 23. Same as Figure 14, but for accumulated precipitation amount in multiply seeded case.

seems to be due to the differences in the graupel mass mixing ratio increase (Figures 19d and 24d). The maximums of rain mass mixing ratio increase under the seeded clouds correspond well with the maximums of the increase of the graupel mass mixing ratio and the graupel increase in the multiply seeded cloud is larger than that in the ordinarily seeded cloud.

The distribution of the cloud water mass mixing ratio 70 min after the beginning of the multiple seeding is shown in Figure 25a. The seeded cloud region is between 139.3°E and 139.5°E, as in the ordinarily seeded cloud case. The cloud top height is about 5.5 km at 139.3°E and a little lower, about 0.1 km, than that of the ordinarily seeded cloud (Figure 20a). The cloud mass mixing ratio at 139.3°E is 0.7 g kg^{-1} at its maximum and is a little less than that in the ordinarily seeded cloud. The magnitude of the maximum of the snow mass mixing ratio increase in the multiply seeded cloud is close to that in the ordinarily seeded cloud, but the increase in the snow area in the multiply seeded cloud is much larger (Figures 25b and 20b). The maximum snow mass mixing ratio increase in the multiply seeded cloud is located west of that in the ordinarily seeded cloud and in an area of cloud water (Figure 25a). For the distributions of the cloud ice mass mixing ratio increase and temperature changes, the area influenced by the seeding is much wider in the multiply seeded cloud than that in the ordinarily seeded one (Figures 25c, f, 20c, f). The structure of the differences in wind shows slightly larger areas of ascending and descending flow in the multiply seeded cloud than in the ordinarily seeded cloud between 139.3°E and 139.5°E. The graupel mass mixing ratio decreases in the ordinarily seeded cloud, while it is slightly increased and decreased in different areas in the multiply seeded cloud (Figures 20d and 25d).

The rain mass mixing ratio increase is larger for the multiply seeded cloud than the ordinarily seeded cloud (Figures 20e and 25e). The comparatively wider area of increased rain mass mixing ratio and stronger intensity of the increase observed under the multiply seeded cloud than the ordinarily seeded cloud (Figures 25e and 20e) are results of the differences in the snow and graupel mass mixing ratios described above. The distribution of the differences in the total mass mixing ratio in the multiply seeded case is shown in Figure 25g. A wider positive area and narrower negative area of the differences are observed in this case than in the ordinarily seeded case (Figure 22a). The wider positive area and narrower negative area are due to the larger increased snow area described above.

Evolution of a seeded cloud at temperatures colder than −8°C

Cloud ice particles are assumed to be dispersed only in

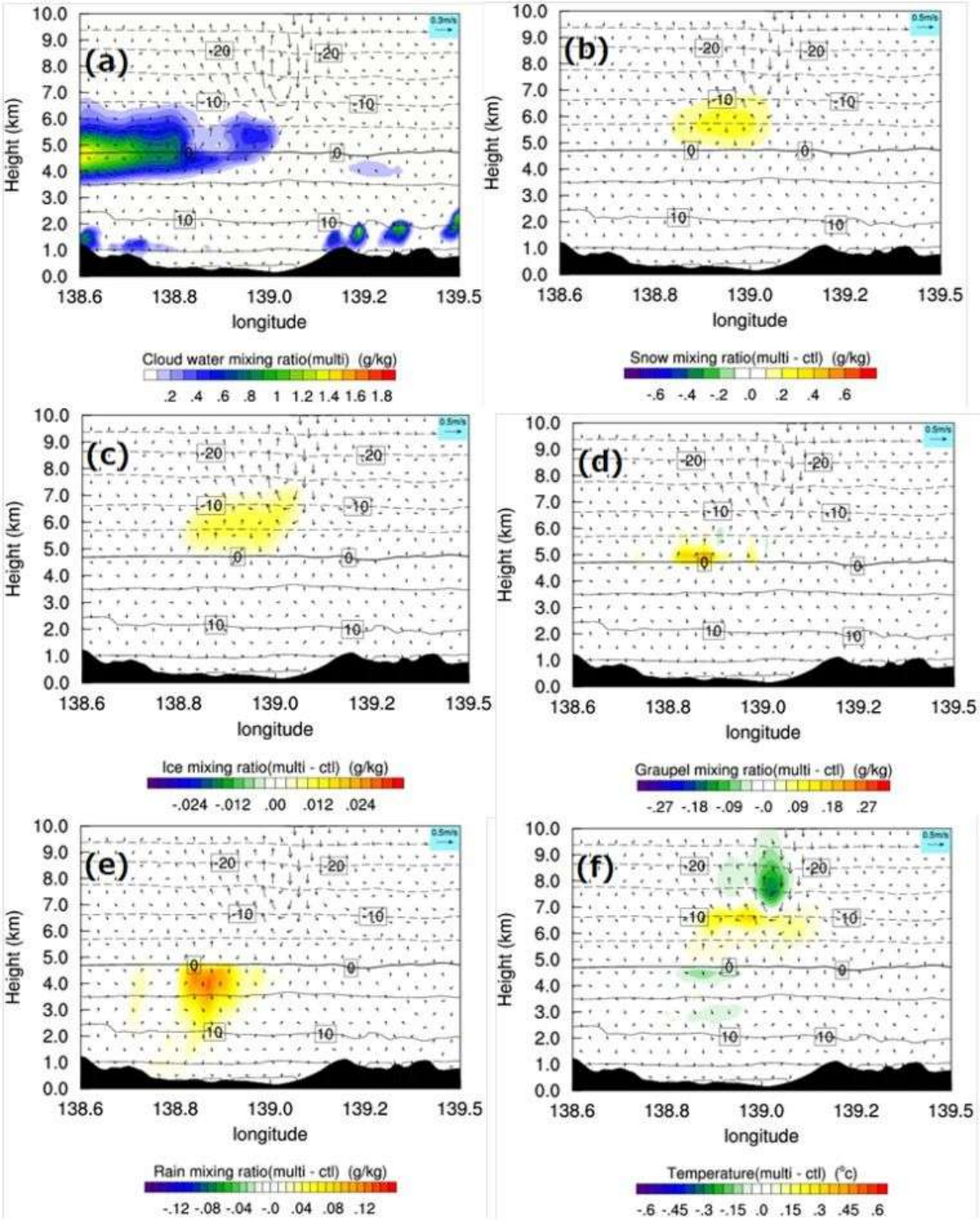

Figure 24. Same as Figure 19, but for 30 min after the beginning of the multiple seeding.

areas of a cloud colder than −8°C to estimate the seeding effects using AgI as the seeding agent, because seeded AgI can generate a similar number of ice crystal nuclei as dry ice in atmospheres of around −8°C, as described in section 2. The number of dispersed cloud ice particles is assumed to be the same as in the weakly seeded case: 1.0×10^{16}. The distribution of the cloud water mass mixing ratio 30 min after seeding is shown in Figure 26a and is not greatly different from that in the control case in Figure 12c. The difference is slightly greater at a height of 6 km between 138.85°E and 139.0°E where the cloud water mass mixing ratio is lower (about 0.16 g kg^{-1}) than in the control case cloud (Figure 26b). The maxima of the snow and cloud ice mixing ratio increases are only 0.12 g kg^{-1} and 0.001 g kg^{-1}, respectively (Figure 26c, d). The cloud ice increase only

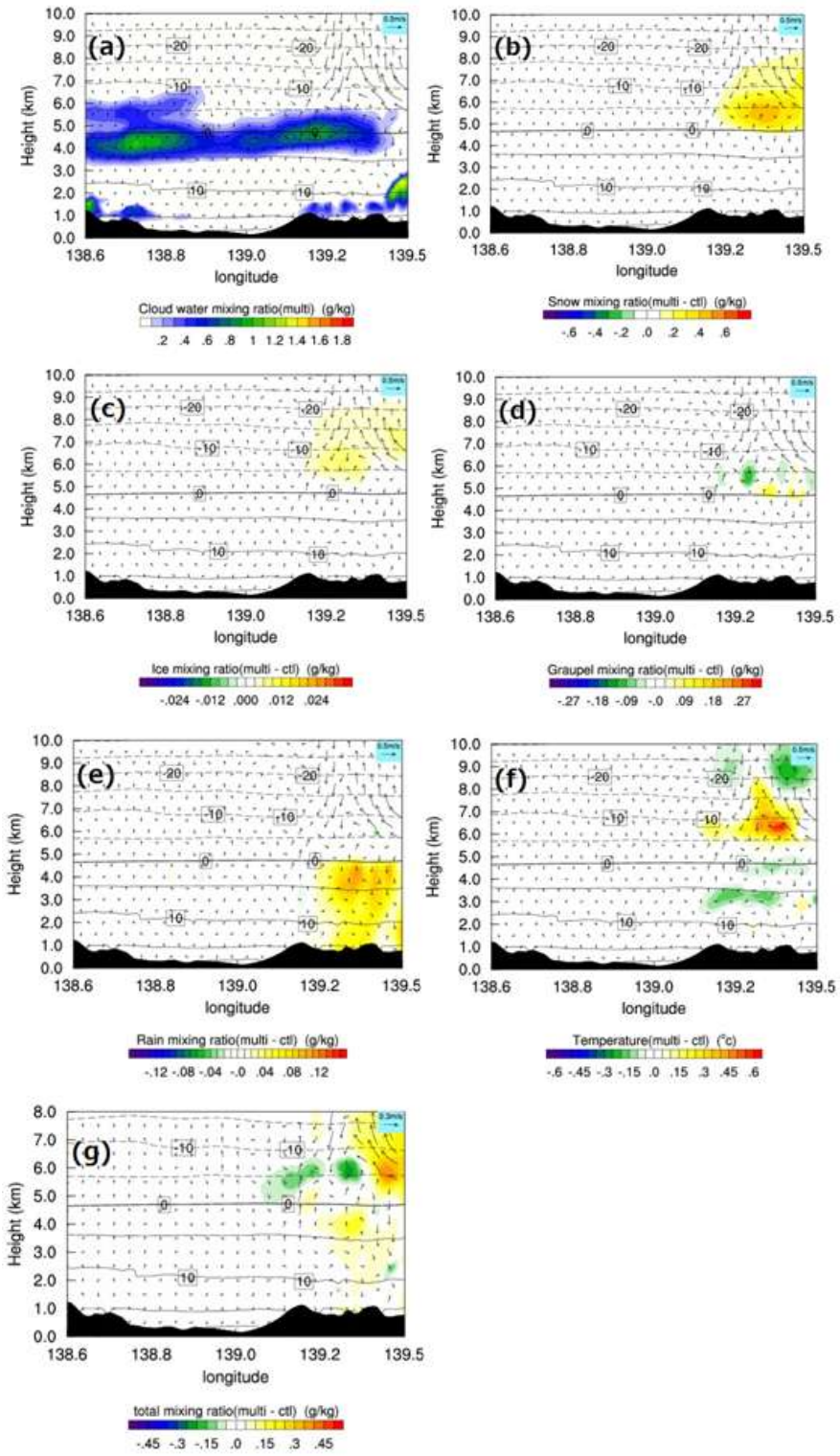

Figure 25. Same as Figure 24, but for 70 min after the beginning of the multiple seeding. Figure 25g shows distribution of sum of differences in water mass mixing ratio without water vapor as Figure 16f.

occurs in areas colder than −5°C, while it occurs at temperatures colder than 0°C in the weakly seeded cloud. The maximum snow increase is also found at temperatures colder than −5°C. The changes in the

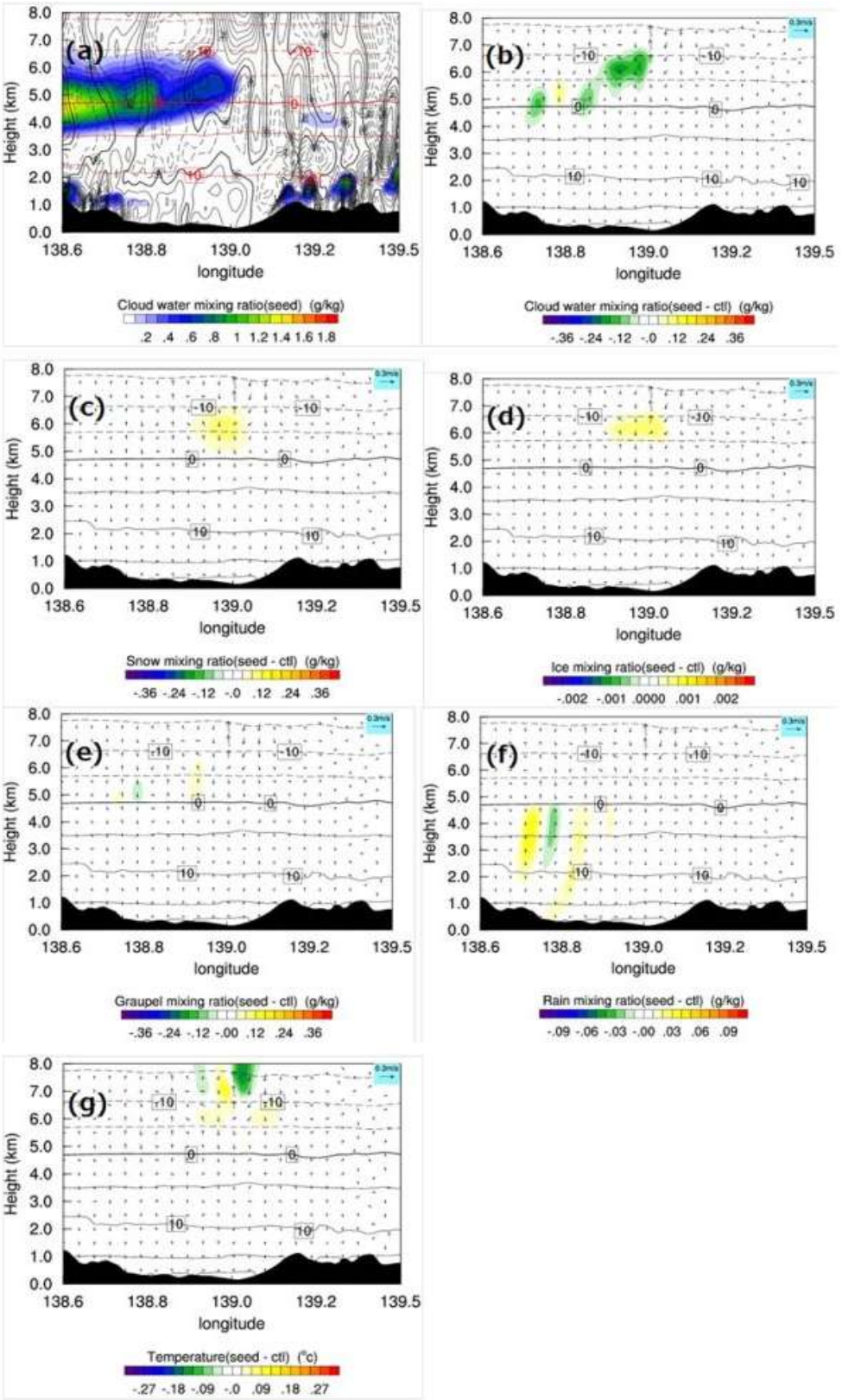

Figure 26. Same as Figure 19, but for 30 min after seeding in upper portion of the cloud than -8°C level. (a) distribution cloud water mass mixing ratio and vertical wind component as Figure 12, (b) differences in cloud water mass mixing ratio. c, d, e, and f show distribution of diffrences in mass mixing ratio of snow, ice, graupel, and rain. (g) shows distribution of differences in temperature.

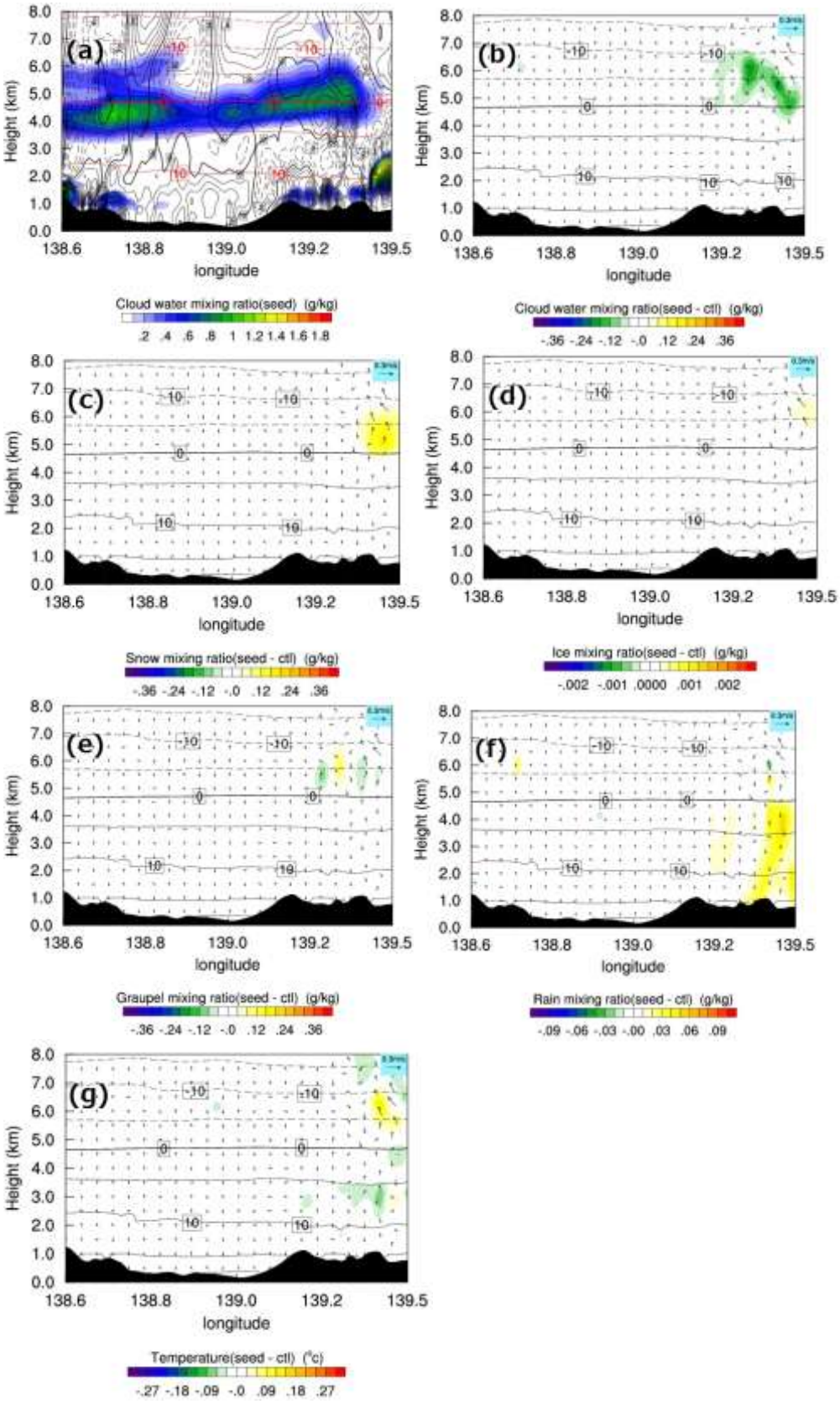

Figure 27. Same as Figure 26, but for 70 min after the cloud seeding only on upper portion than the -8°C level.

atmospheric temperature due to seeding are between −0.12 and 0.15°C (Figure 26g), while they are between −0.3 and 0.4°C in the weakly seeded cloud. The differences in the wind velocity do not differ greatly. The rain mass mixing ratio increases at 138.7°E and 138.9°E, and decreases at 138.75°E. The positions of the increase and decrease roughly correspond with those of the graupel mass mixing ratio (Figure 26e, f). The effects of the seeding in only the upper portion of the cloud are less than those on the weakly seeded cloud. This is assumed to be due to the fact the seeding is limited to a far smaller and higher area in the cloud.

The distribution of the cloud water mass mixing ratio 70 min after seeding is shown in Figure 27a and it is not greatly different from that of the control case in Figure 12f, except that the mixing ratio at a height of 5 km at 139.3°E in this case is a little less than that in the control case. This result is seen more clearly in Figure 27b, which shows the distribution of the differences in cloud water mass mixing ratio between this case and the control case. The mixing ratio is decreased by around 0.16 g kg^{-1} over the area between 139.3°E and 139.4°E in this case. The increase in the snow and cloud ice mass mixing ratio are 0.20 and 0.00075 g kg^{-1}, as shown in Figure 27c and d, respectively. The increase in the ice mass mixing ratio is still above −5°C level but the increase in the snow mass mixing ratio area falls till 0°C level as in the weak seeding case (Figure 16b). The rain mass mixing ratio increase due to seeding is up to 0.05 g kg^{-1} and the magnitude of atmospheric temperature change is 0.12°C, as seen in Figures 27f and g. The position of the rain mass mixing ratio increase corresponds well with the increased snow mass mixing ratio area (Figure 27c). The magnitudes of changes in the meteorological elements are still less than those in the weakly seeded case.

CONCLUSION

In this study, the accumulated precipitation amount in the catchment area is investigated because it is not possible to consider the efficiency of different precipitation methods in terms of the accumulated precipitation amounts from seeding until cloud dissipation, as the innermost domain is not wide enough to simulate the cloud until dissipation.

The precipitation amount over the catchment area is largest in the multiply seeded case and it is larger than that in the ordinarily seeded case. Comparing the increase in the rain mass mixing ratios in both cases 70 min after seeding (Figures 20e and 25e), the magnitude and area of the rain mass mixing ratio increase in the multiply seeded case are larger and wider than those in the ordinarily seeded case. The magnitude and area of the snow and graupel mass mixing ratios increases in the multiply seeded case over the rain area are larger and wider than those in the ordinarily seeded case (Figures 20b, d, 25b, d), supporting the conclusions already described. The processes which produced these results are complicated, especially regarding the graupel, and require further analysis. However, it can be seen from the distributions of the cloud water mass mixing ratio and the snow mass mixing ratio increase that the cloud water mass mixing ratio area and the snow increase area are slightly misaligned in the ordinarily seeded case (Figure 20a, b), while they are more overlapped in the multiply seeded case and the cloud water mass mixing ratio is lower at 139.3°E (Figure 25a, b). It is supposed that the ordinarily seeded ice crystals tend to be concentrated through convection stimulated by the released latent heat from freezing and the concentrated ice crystals consume the cloud water to generate snow. Thus, the concentration of ice crystals forms a structure where the cloud water mass mixing ratio area and the snow mass mixing ratio increase area are misaligned, inhibiting further growth of snow particles. On the other hand, the seeding area in the multiple seeding method moves with the cloud regardless of the movement generated by the convection caused by seeding. Thus, the ice crystals in the multiply seeded cloud are not concentrated as tightly as in the ordinarily seeded cloud and the seeding agent can affect the cloud over a wider area than in the ordinarily seeded cloud. As a result, multiple seeding can influence the cloud over a wider area and more effectively than in the ordinarily seeded cloud case.

The distribution of the differences in the total mass mixing ratio shown in Figures 16f, 22a and 25g refers to the sum of the cloud water, snow, cloud ice, graupel, and rain differences in mass mixing ratios between the seeded clouds and the cloud in the control case, as described before. In other words, it is the sum of differences in the water mixing ratio, excluding the water vapor. The difference in the total mass mixing ratio is expected to be negative in the cloud and positive in the rain catchment area if a hygroscopic seeding method is used, because hygroscopic seeding is expected to convert cloud water to rain. Also, the difference is expected to be zero if the glaciogenic seeding converts the cloud water into snow or graupel and the snow and the graupel do not fall at the generated position. However, the snow and the graupel generated through glaciogenic seeding always fall away from the cloud and the difference tends to become negative in the cloud and positive in the rain area as with hygroscopic seeding. Then, the area with positive difference in the total mass mixing ratio means that snow is newly generated in an ascending flow, and this is one of the characteristics of a cloud exposed to glaciogenic seeding. The magnitude of the positive difference is not significant in the weakly seeded case (Fig. 16f) but is notable in the ordinarily and multiply seeded cases (Figures 22a and 25g) compared with the distribution of the cloud water mass mixing ratio in the control case (Figure 12f). It is recognized that from

a third to a quarter of the increased snow mass mixing ratio is comparable to the differences in the total mass mixing ratio, and this shows that newly generated snow in the ascending flow due to the released latent heat from freezing is important to increase the snow mixing ratio. The newly generated snow is expected to enhance precipitation in the catchment area and in areas where the seeded cloud passes through thereafter.

As described earlier, the snow increase area is formed at heights above the −5°C level 30 min after seeding in the seeded cloud when only the upper cloud portion above −8°C level is seeded. Under these conditions, only a narrow area of the cloud is affected by the ice crystals generated through the seeding, and the seeding effects are weak. The area with an increased amount of snow descends into the cloud to the 0°C level 70 min after seeding. The cloud is expected to be influenced by the snow as much as the cloud in the weakly seeded case. The effect of seeding may be as great as in the weakly seeded case after a sufficiently long time has passed, while the seeding effects in this case are less than those in the weakly seeded case in this study as described above.

An additional characteristic of glaciogenic seeding is presented in this study. This characteristic is that the increased rain mass mixing ratio with the weak seeding method can affect the underlying cloud to enhance precipitation, as described earlier. This result shows the effectiveness of glaciogenic seeding conducted in a relatively warm cloud which has a super-cooled portion near the top. In this case, it is supposed that the increase in precipitation by the glaciogenic seeding conducted on the super-cooled portion of the cloud will be more effective as the raindrops are falling through the warmer lower portion of the cloud as expected before.

REFERENCES

Bruintjes, R. T. (**1999**). A review of cloud seeding experiments to enhance precipitation and some new prospects. Bull Amer Meteor Soc, 80: 805-820.

Cooper, W. A., and **Bruintjes**, R. T. (**1997**). Calculation pertaining to hygroscopic seeding. J Appl Meteor, 36: 1449–1469.

Dennis, A. S., and **Orville**, H. D. (**1997**). A new look at the Israeli cloud seeding experiments. J Appl Meteor, 36: 277-278.

English, M., and **Marwitz**, J. D. (**1981).** A comparison of AgI and CO_2 seeding effects in Alberta cumulus clouds. J Appl Meteor, 20: 483-495.

Fletcher, N. H. (**1962**). The physics of rainclouds. Cambridge University Press. 386 pp.

Fukuta, N. (**1996**). Project mountain valley sunshine-progress in science and technology. J Appl Meteor, 35: 1483-1493.

Fukuta, N., Schmeling, W. A., and Evans, L. F. (**1971**). Experimental determination of ice nucleation by falling dry ice pellets. J Appl Meteor, 10: 1174-1179.

Garstang, M., Bruintjes, R., Serafin, R., Orville, H., Boe, B., Cotton, W., and Warburton, J. (**2004**). Weather modification: Finding common ground. Bull Amer Meteor Soc, 85: 647-655.

Hobbs, P. V., and **Politovich**, M. K. (**1980**). The structures of summer convective clouds in eastern Montana. II: effects of artificial seeding. J Appl Meteor, 19: 664-675.

Holroyd, E. W. Ⅲ, and Jiusto, J. E. (**1971**). Snowfall from a heavy seeded cloud. J Appl Meteor, 10: 266-269.

Marwitz, J. D., and **Stewart**, R. E. (**1981**). Some seeding signatures in Sierra storms. J. Appl. Meteor., 20: 1129-1144.

Mather, G. K., Terblanche, D. E., Steffens, F. E., and Fletcher, L. F. (**1997**). Results of the South Africa cloud-seeding experiments using hygroscopic flares. J Appl Meteor, 36: 1433–1447.

Milbrandt, J. A., and **Yau**, M. K. (**2005a**). A multimoment bulk microphysics parameterization. Part I: Analysis of the role of the special shape parameter. *J. Atmos. Sci.*, 62, 3051-3064.

Milbrandt, J. A., and **Yau**, M. K. (**2005b**). A multimoment bulk microphysics parameterization. Part Ⅱ: A proposed three-moment closure and scheme description. J Atmos Sci, 62, 3065-3081.

Miller, J. R., Jr., Boyd, E. I., Schleusener, R. A., and Dennis, A. S. (**1975**). Hail suppression data from western North Dakota, 1969-1972. J Appl Meteor, 14: 755-762.

Mlawer, E. J., Taubman, S. J., Brown, P. D., Iacono, M. J., and Clough, S. A. (**1997**)**.** Radiative transfer for inhomogeneous atmosphere: RRTM, a validated correlated-k model for the long-wave. J Geophys Res, 102(D14): 16663-16682.

Morrison, H., and **Milbrandt**, J. (**2011**). Comparison of two-moment bulk microphysics scheme in idealized supercell thunderstorm simulations. Mon Weath Rev, 139: 1103-1130.

Rangno, A. L., and **Hobbs**, P. V. (**1995**). A new look at the Israeli cloud seeding experiments. J Appl Meteor, 34: 1169-1193.

Rangno, A. L., and **Hobbs**, P. V. (**1997**). Reply. J Appl Meteor, 36: 279.

Rogers, R. R., and **Yau**, M. K. (**1989**). A short course in cloud physics. 3rd ed. Pergamon Press. p. 16.

Rosenfeld, D., (**1997**). Comments on "A new look at the Israeli cloud seeding experiments". J Appl. Meteor, 36: 260-271.

Rosenfeld, D., and **Woodley**, W. L. (**1989**). Effects of cloud seeding in west Texas. J Appl Meteor, 28: 1050-1080.

Schaefer, V. J. (**1946**). The production of ice crystals in a cloud of supercooled water droplets, Science, 104: 457–459.

Seto, J., Tomine, K., Wakimizu, K., Nishiyama, K. (**2011**). Artificial cloud seeding using liquid carbon dioxide: Comparisons of experimental data and numerical analyses. J Appl Meteor, 50: 1417-1431.

Shimada M., Tomine, K., and Nishiyama, K. (**2016**). Model analysis of radar echo split observed in an artificial cloud seeding experiment. J Meteor Res, 30: 386-400.

Silverman, B. A. (**2001**). A critical assessment of glaciogenic seeding of convective clouds for rainfall enhancement. Bull Amer Meteor Soc, 82: 903-923.

Stewart, R. W. (**1986**). Weather modification in Alberta. Summary report and recommendations.

Tessendorf, S. A., Bruintjes, R. T., Weeks, C., Wilson, J. W., Knight, C. A., Roberts, R. D., Peter, J. R., Collis, S., Buseck, P. R., Freney, E., Dixon, M., Pocernich, M., Ikeda, K., Axisa, D., Nelson, E., May, P. T., Richter, H., Piketh, S., Burger, R. P., Wilson, L., Siems, S. T., Manton, M., Stone, R. C., Pepler, A., Collins, D. R., Bringi, V. N., Thurai, M., Turner, L., and McRae, D. (**2012**). The Queensland Cloud Seeding Research Program. Bull Amer Meteor Soc, 93: 75–90.

Tomine, K., Shimada, M., Wakimizu, K., and Nishiyama, K. (**2015**). An example of canal in a thick cloud induced by massive seeding using liquid carbon dioxide. J Meteor Res, 29: 682-690.

Vonnegut, B. (**1947**). The nucleation of ice formation by silver iodide. J Appl Phys, 18: 593-595.

Wakimizu, K., Nishiyama, K., Suzuki, Y., Tomine, K., Yamazaki, M., Isimaru, A., Ozaki, M., Itano, T., Naito, G., Fukuta, N., (**2002**). A low level penetration seeding experiment of liquid carbon dioxide in a convective cloud. Hydrol Processes, 16: 2239-2253.

Woodley, W. L., Jordan, J., Barnston, A., Simpson, J., Biondini, R., and Flueck, J. (**1982**). Rainfall results of the Florida area cumulus experiment, 1970-76. J Appl Meteor, 21: 139-164.

Zoljoodi, M. and Didevarasl, A. (**2013**). Evaluation of cloud seeding project in Yazd Province of Iran using historical regression method (case study: Yazd 1 cloud seeding project, 1999). Nat Sci, 5: 1006-1011.

Citation: Saito, T., Sashihara, R., Komatsuzaki, K., and Tomine, K. (2017). Numerical experiments on glaciogenic artificial cloud seeding conducted in a stable cloud. Afr J Eng Res, 5(3): 54-82.